An Autoinhibited Conformation of the DnaB-Replicative Helicase – phage λP Helicase Loader Complex

†Dhanjai Brown[1,2], †Abhipsa Shatarupa[1,2], Paul Dominic B. Olinares[5], Jillian Chase[1,2], Eta Isiorho[6], Brian T. Chait[5], and *David Jeruzalmi[1,2,3,4]

[1]Department of Chemistry and Biochemistry, City College of New York, New York, NY 10031, USA.

Ph.D. Programs in Biochemistry[2], Biology[3], and Chemistry[4], The Graduate Center of the City University of New York, New York, NY 10016, USA.

[5]Laboratory of Mass Spectrometry and Gaseous Ion Chemistry, The Rockefeller University, New York, New York 10065, USA

[6]Structural Biology Initiative, CUNY Advanced Science Research Center, New York, NY 10031, USA

*To whom correspondence should be addressed: 212-650-6062; dj@ccny.cuny.edu

†These authors contributed equally.

Graphical Abstract

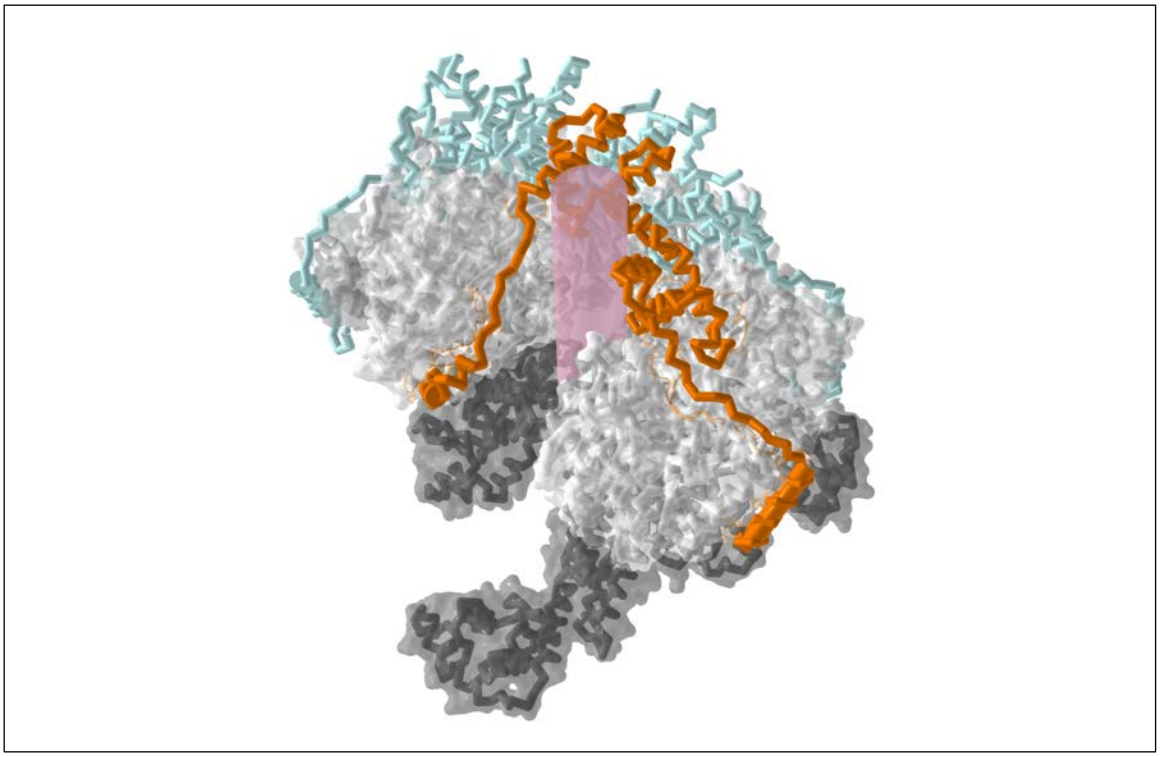

The autoinhibited configuration of the DnaB helicase λP loader complex. Interaction with the loader reconfigures the helicase, depicted in the ribbon format and under a transparent surface, into an open spiral, with its internal chamber exposed to solvent. One copy of the λP loader binds across the single breached interface in DnaB, effectively blocking the path into the inner chamber. The pink cylinder represents the expected path of ssDNA through DnaB.

Abstract

Replicative helicases require loader proteins for assembly at origins of DNA replication. Multiple copies of the bacteriophage λP loader bind to the *E. coli* DnaB replicative helicase and trigger its reconfiguration into a right-handed open spiral wherein an internal chamber becomes accessible to physiological single stranded DNA. In the 2.84 Å model of the DnaB – λP complex, the pentameric λP ensemble adopts an asymmetric configuration; one copy of λP, which is visualized in full, binds at the top and bottom of the open DnaB spiral; the presence of a single breach in the DnaB open spiral implies that the remaining four copies of λP must adopt distinct conformations. DnaB's internal chamber remains accessible to ssDNA, however, the λP protomer whose binding site spans the breach effectively blocks the path into the inner chamber to give rise to an autoinhibited configuration for the complex. Although the path to the inner chamber is blocked, the BP complex, nevertheless, binds ssDNA, and we suggest that the path for ssDNA lies outside the DnaB ring. Comparisons of the λP and DnaC complexes of the DnaB helicase shed new light on how the two loaders, though unrelated in structure, converged on the same ring-opening mechanism. Our structure suggests the conformation changes that accompany recruitment to the initiator protein complex at the replication origin.

Introduction

Replicative helicases, and the loader proteins that assemble them onto DNA, are found in the chromosomal replicating systems from all cellular domains of life [1–10]. Replicative helicases are oligomeric entities that circumscribe an inner chamber into which single-stranded DNA (ssDNA) is loaded. However, given that DNA is effectively an infinitely long polymer with no free ends, assembly of replicative helicases on DNA requires specialized loader proteins; assembly takes place during the initiation phase of DNA replication. In bacteria, the replicative helicase, termed DnaB in most bacteria (henceforth: DnaB) or DnaC in *B. subtilis*, is a homohexamer that encircles and translocates on the lagging strand at the replication fork, while excluding the second strand from the inner chamber. ATP-dependent translocation by DnaB mediates separation of duplex DNA into templates for replication. Extensive literature provides insights into the structure and function of helicase loaders in bacteria, including *E. coli* DnaC, phage λP, *B. subtilis* DnaI, phage T4 gene 59, phage SPP1 G39P, phage P2 B, DciA, and DopE [1, 7, 11–22].

Hexameric *E. coli* DnaB is a two-tiered, ring-shaped ensemble with an internal chamber that is ordinarily sealed to entry by ssDNA [23–25]. Each DnaB protomer is formed out of two domains: an amino-terminal domain (NTD) and a carboxy-terminal domain (CTD); the NTD and CTD of each DnaB subunit are linked by a linker helix (LH) element. In the assembled hexamer, pairs of amino-terminal domains engage in a dimeric arrangement and three of these dimers assemble into a trimeric configuration that represents one of DnaB's layers; the NTD layer circumscribes the DNA binding channel and provides binding sites for

DNA primase during the elongation phase of DNA replication. The second of DnaB's layers is formed out of six carboxy-terminal domains (CTD), which, in contrast to the NTD layer, exhibits a pseudo-sixfold arrangement. Each CTD harbors a helical element, termed the docking helix (DH), which packs against the LH element of an adjacent CTD [23–25]. DnaB, a superfamily 4 helicase, binds ATP at CTD interfaces; the Walker A and Walker B motifs for this composite site are furnished by one CTD and the arginine finger-beta-hairpin motif by the adjacent CTD. The residues that contact the phosphate backbone of ssDNA within the inner chamber of DnaB are also found on the CTD [26]; it has been suggested that interplay between the arginine finger-beta-hairpin motif and the ssDNA binding loops links ssDNA binding with ATP hydrolysis [26]. The NTD and CTD layers are found in two arrangements, termed: dilated and constricted; in addition to differently sized inner chambers, these two states feature distinct arrangements that give rise to divergent inter-subunit contacts.

Loading of the bacterial DnaB helicase onto origin DNA occurs at the nexus of two pathways that assemble two sub-complexes; these, then, coalesce, into the complete initiation complex at the replication origin [27–29]. The first sub-complex is the oligomeric initiator protein complex (*E. coli:* DnaA or phage λ: O) formed at the cognate replication origin; a critical product of this complex is the initial melting of the origin's DNA unwinding element (DUE). The second sub-complex is assembled by capture and remodeling of the DnaB helicase by the helicase loader. These two pathways converge with delivery of the loader-bound helicase to the origin; ssDNA produced by the initiator – origin DNA complex is suggested to enter

the opened inner chamber of DnaB. The resulting initiator-helicase-loader complex at the origin is stabilized by contacts between initiator, helicase, and loader [1, 8, 30, 31]. A series of additional binding and remodeling events culminate in assembly of a pair of replication forks [27–29, 32, 33]. In the phage λ system, activation of the helicase also requires engagement of the host heat shock factors DnaJ, DnaK, and GrpE [34–37].

Three schemes for helicase loading have been described, termed here as: (1) ring-opening, (2) ring-forming, or (3) ring-closing [10, 38, 39]. These schemes are organized around the structure of the helicase prior to loading. In the ring-opening scheme, the hexameric helicase exhibits a closed ring configuration; during helicase loading one of the six interfaces is breached to permit entry of ssDNA into the internal chamber; the *E. coli* DnaC and bacteriophage λP loaders [40–42] implement this scheme. In the ring-forming scheme, DnaB subunits are assembled around DNA by the *B. subtilis* DnaI loader into the active helicase [12]. The ring-closing scheme is seen with the Rho and MCM2-7 helicases wherein the hexameric rings are pre-opened; ring closure takes place with entry of the nucleic acid substrate into the inner chamber and involves other factors [10, 43, 44].

Here, we focus on the ring-opening loaders where binding and remodeling events associated with loading and activating the DnaB helicase can also be considered to transition through four stages (stages I-IV) [23–26, 40–42]. The isolated stage I helicase adopts a closed planar configuration with the NTD and CTD layers either in the dilated or constricted shape. In stage II, DnaB has been captured and remodeled by the loader (*E. coli:* DnaC or phage λ: P) into an open

right-handed spiral, with both tiers in the constricted conformation [40, 41, 45]. Remodeling creates openings in DnaB's two tiers of sufficient size to permit access to the inner chamber by ssDNA. The ATPase and translocase activities of DnaB are suppressed when bound by the loader [56,58,69–71]. Engagement with initiator-produced ssDNA by the helicase•loader complex leads to stage III; ssDNA is bound by the loader and within a remodeled DnaB spiral whose inner chamber is now topologically closed; the CTD tier features the constricted state, while the NTD layer is dilated [41]. Expulsion of the loader accompanies transition to stage IV, which is suggested to be the translocating form of DnaB [26, 41].

Analyses of structures of *E. coli* DnaB helicase bound in distinct complexes to the *E. coli* DnaC (BC) and phage λP (BP) loaders shed considerable light on mechanisms of helicase opening, ssDNA entry, followed by sealing of the inner chamber of DnaB with ssDNA trapped inside [40, 41, 45]. Although unrelated in sequence or structure, the two loaders feature a similar overall architecture: a globular domain attached to an element termed the lasso/grappling hook. Differing numbers of loader subunits (DnaC: 6; λP: 5) in the BC and BP complexes engage the CTD layer of DnaB to trigger the change from the closed planar to closely related open spiral configurations. Remarkably, the only region of structural resemblance between the two loaders is the alpha helix at the tip of the lasso/grappling hook that is positioned between the LH and DH helices of two adjacent DnaB subunits. Amazingly, however, the protein chain direction of these elements (λP: C-N; DnaC: N-C) diverges, implying that chain direction is not

important for triggering helicase opening. This unusual feature of λP and DnaC reflects a type of molecular mimicry that emerged from convergent evolution.

Analysis of the structure of the BP complex by cryogenic-electron microscopy (cryo-EM) at 4.1 Å provided a great deal of insights into helicase loading, however, the limited resolution obscured the full structure of the λP loader as only the carboxy-terminal domains of the five protomers were visible in the EM map (EMDB: 7076, PDB: 6BBM [40]). Here, we have extended the resolution of our EM analysis to 2.84 Å. Using a combination of X-ray crystallography and AlphaFold calculations [46, 47], we constructed structures for the five carboxy-terminal domains (domains III/IV, lasso/grappling hook) of λP. The AlphaFold model also enabled the complete structure of one λP monomer to be completely positioned within the BP complex; unexpectedly, this monomer binds across the breach in the DnaB CTD tier. Thus, although the NTD and CTD tiers of DnaB retain their openings, disposition of one λP loader seals the entrance and creates a previously unrecognized autoinhibited conformation of BP. This finding also suggests that the λP ensemble will exhibit a radically asymmetric configuration, with one protomer spanning the single breach in DnaB and the remaining four featuring different, as yet, undescribed, configurations with distinct functions during replication initiation. We find that the λP ensemble stabilizes the open DnaB spiral, as it suppresses ATPase activity. Unlike the DnaC – helicase complex, λP appears to preclude a DnaB configuration compatible with ssDNA binding. Nevertheless, the BP complex binds ssDNA robustly, and we provide evidence that binding may not be taking place within DnaB's inner chamber, implying

existence of an unrecognized intermediate wherein ssDNA may be contacted by λP, or by the outer surface of DnaB, or both.

Materials and Methods

Constructs of the λP helicase loader

The biochemical and structural studies in this work relied upon a large set of constructs of λP (Supplementary Figure 1S and Supplementary Table 1). The sequence inserted for each construct was verified by DNA sequencing (Genewiz/Azenta). Extensive efforts identified soluble domains corresponding to the following constructions: amino acids 105:210, 105:205, 105:215, 105:220, 110:210, 110:215, and 110:233; each construct included an N-terminal (N-His) or C-terminal (C-His) hexahistidine for purification. The following constructs could only be expressed in soluble form when an N-terminal decahistidine tag fused to SUMO (small ubiquitin-like modifier (SUMO)) was included at the amino terminus: 1:30, 1:98, 1:105, 191:233, and 210:233. The construct spanning residues 105:210 provided a sample suitable for X-ray crystallographic studies.

Protein Biochemistry

Full length *E. coli* DnaB•λP complex, *E. coli* DnaB, and entities (Supplementary Figure 1S) containing the *E. coli* DnaB$^{R403A-E404A-G406A}$ mutant were purified using the procedure described in [39], except that 0.2 mM ATP was used instead of 0.5 mM. In addition, full length *E. coli* DnaB and the *E. coli* DnaB$^{R403A-E404A-G406A}$ were further chromatographed over a 320 mL Superdex200 size exclusion column equilibrated in 20 mM HEPES-NaOH, pH 7.5, 450 mM NaCl, 5% glycerol (v/v), 2 mM DTT, 0.5 mM $MgCl_2$, 0.2 mM ATP. DnaB containing fractions

were concentrated to 23.5 mg/mL, aliquoted, flash frozen in liquid nitrogen, and stored at -80°C until use.

The *E. coli* DnaB•λP-C-His complex was first purified over nickel-nitrilotriacetic acid beads (Ni-NTA, Qiagen) equilibrated in 50 mM sodium phosphate, pH 7.6, 500 mM NaCl, 10% glycerol (v/v), and 5 mM β-mercaptoethanol (BME). After sequential washing the Ni-NTA beads with 25 mM, 50 mM, and 100 mM imidazole in the equilibration buffer, partially purified DnaB•λP-C-His complex was eluted using successive washes containing 250 mM, 500 mM, and 500 mM imidazole in the equilibration buffer. The complex was further purified using methyl hydrophobic interaction chromatography as described in [40]. Lastly, the complex was concentrated to ~9 mg/mL, aliquoted, flash frozen in liquid nitrogen, and stored at -80°C until use.

The *E. coli* DnaB•λP-102-233-C-His complex was purified using a combination of NiNTA as described above, Q-sepharose chromatography as described in [40] , followed by chromatography over Superdex200 as described above.

λP constructs encompassing residues 105:210 and 110:233 were expressed in *E. coli* BL21 (DE3) cells as described in [40], except that the induction proceeded at 16°C for 16 hours. λP105:210 substituted with selenomethionine (SeMet) was prepared for X-ray crystallographic studies as described in [48]. Cells expressing N-His-λP105:210 and N-His-λP110:233 were lysed by sonication (60% amplitude; 3 min; 0.3 secs on, 0.6 secs off, Fisher Scientific Model 500). Both constructs were recovered in the lysis supernatant, purified over Ni-NTA as

described above, and over Superdex200 equilibrated in 100 mM NaCl, 10mM TRIS-HCl pH 7, 5% glycerol (v/v), and 5mM BME. Fractions containing N-His-λP105:210 were concentrated to 3.5 mg/mL, aliquoted, flash frozen in liquid nitrogen, and stored at -80°C until use.

Several N-His-SUMO fused λP constructs (1:30, 1:98, 1:105, 191:233 and 210:233) were expressed in soluble form, but not purified. Instead, we used crude preparations of these constructs in so-termed Ni-NTA pull-down experiments with *E. coli* DnaB. The pull-down experiments, summarized in Figure 3 and in Supplementary Figure 2S, were conducted like the Ni-NTA purification of the *E. coli* DnaB•λP-C-His complex above except that 150 µL of beads and 1 mL of crude protein solution were used, and the beads were washed twice with 60 mM imidazole and eluted with 300 mM imidazole, both in 50 mM potassium phosphate pH=8.0, 500 mM NaCl, 10% glycerol (v/v), and 100 µM ATP. Each pull-down experiment was analyzed by SDS-PAGE of the load, flow-through, wash, and eluted fractions.

All of the above procedures were performed at 4°C.

X-ray structure determination of λP domain III (residues 105 – 210)

N-His-λP105:210 in 100 mM NaCl, 10 mM TRIS-HCl pH 7, 5% glycerol (v/v), and 5 mM BME was thawed on ice and further concentrated to ~3.5 mg/mL (> 200 µM). High-throughput vapor diffusion (sitting drop) crystallization trials were performed on an Art Robbins Gryphon liquid handling robot utilizing commercial screens (Qiagen) in The Macromolecular Crystallization Facility (MCF) of the Structural Biology Initiative at the Advanced Science Research Facility at the City University of New York. Crystals of λP105:210 were prepared using the sitting

drop vapor diffusion method by mixing either 0.1, or 0.2, or 0.4 μL of the protein solution and 0.2 μL of a series of commercially available crystallization screens (Qiagen). Conditions that provided initial hits were optimized using bespoke screens prepared at the MCF. Optimized crystals for X-ray diffraction were grown at room temperature in a buffer consisting of 3 M – 4 M NaCl with 0.1 M HEPES-NaOH, pH 7 – 8 and required 7 days to form. SeMet-derivatized crystals were grown in the same manner. For X-ray diffraction, crystals (>70 μm) were cryoprotected by adding 0.2 μL LV CryoOil (MiTeGen) directly onto the crystallization drop prior to flash freezing in liquid nitrogen.

Diffraction data for native and SeMet-derivatized N-His-λP105:210 crystals were recorded at cryogenic temperatures at the 24-ID-E and 24-ID-C (respectively) beamlines at the Northeastern Collaborative Access Team (NECAT) Center for Advanced Macromolecular Crystallography at the Advanced Photon Source at Argonne National Laboratory. Data from native crystals were measured using a wavelength of 0.97918 Å to Bragg spacings of 1.86 Å. Data from SeMet-derivatized crystals were measured at the Se-edge (12,662 eV, λ = 0.97918 Å), to Bragg spacings of 1.86 Å. Both native and derivatized λP105:210 crystallized in space group $P3_121$, with the following cell parameters: a = 49.731, b = 49.731, c = 70.772, alpha = 90°, beta = 90°, and gamma = 120° (Supplementary Table 2). The Matthews coefficient [49] implied presence of one copy of λP105:210 in the crystallographic asymmetric unit.

Diffraction images were integrated and scaled with HKL2000 [50]. Efforts to determine phases of the λP105:210 structure using molecular replacement and

various search models derived from the cryo-EM structure of the DnaB-λP complex did not provide a reliable solution. However, the structure was readily determined, using the single anomalous dispersion (SAD) method on the SeMet substituted crystals as implemented in the Autosol in the Phenix suite [51]. AutoBuild and phenix.refine as well as visualization with Coot [52] aided development of the final model that consists of residues 119 to 192 (residues 105 to 118 and 193 to 210 could not be visualized) and featured a crystallographic R factor, R_{work}/R_{free} of 0.23/0.24. In all cases, initial models were improved using several rounds of model building and refinement as implemented in Phenix [51].

Native mass spectrometry (MS)

The protein samples (DnaB, $DnaB^{R403A-E404A-G406A}$, and DnaB•λP-C-His) that had been stored frozen in 20 mM HEPES-NaOH pH 7.5, 450 mM NaCl, 0.5 mM $MgCl_2$, 2 mM DTT, 5% glycerol (v/v), and 0.2 mM ATP were thawed and diluted to 5 μM (assuming the DnaB complex is a hexamer and the DnaB-λP assembly is mainly B_6P_5). The ssDNA constructs (Genewiz, LLC) included: (1) a 43-nucleotide sequence (5'- TGACGAATAATCTTTTCTTTTTTCTTTTGTAATAGTGTCTTTT-3') derived from the DNA unwinding element (DUE) of Oriλ [53] and (2) a 45-mer thymidylate homopolymer (poly-dT). For the DNA binding experiments, 6 μM ssDNA (1.2 x molar ratio relative to the protein complex) was used. The samples with or without ssDNA were then incubated with 0.5 mM ATP on ice for 20 min and buffer-exchanged into nMS solution (450 mM or 500 mM ammonium acetate, pH 7.5, 0.5 mM magnesium acetate, 0.01% (w/v) Tween-20) using Zeba microspin desalting columns (Thermo Scientific) with a 40-kDa molecular weight cut-off (MWCO).

For nMS analysis, an aliquot (2 – 3 μL) of the buffer-exchanged sample was loaded into a gold-coated quartz capillary tip that was prepared in-house and was electrosprayed into an Exactive Plus EMR instrument (Thermo Fisher Scientific) using a modified static nanospray source [54]. The nMS parameters used included: spray voltage, 1.20 – 1.25 kV; capillary temperature, 125 – 150 °C; S-lens RF level, 200; resolving power, 8,750 at m/z of 200; AGC target, 1 x 10^6; number of microscans, 5; maximum injection time, 200 ms; in-source dissociation (ISD), 0 – 10 V; injection flatapole, 8 V; interflatapole, 4 V; bent flatapole, 4 V; high energy collision dissociation (HCD), 200 V; ultrahigh vacuum pressure, 5.3 – 6.7 × 10^{-10} mbar; total number of scans, 100. Mass calibration in positive EMR mode was performed using cesium iodide. Raw nMS spectra were visualized using Thermo Xcalibur Qual Browser (version 4.2.47). Data processing and spectra deconvolution were performed using UniDec version 4.2.0 [55, 56]. The following parameters were used for data processing: background subtraction (if applied), subtract curve 10; smooth charge state distribution, enabled; peak shape function, Gaussian; beta setting (degree of Softmax distribution): 20. The observed deviations of the measured mass from the expected mass ranged from 0.03% to 0.13% and were due to peak broadening mainly from nonspecific magnesium adduction. All mass spectrometric data were measured by PDBO in the laboratory of BTC.

ATPase rate measurements

An NADH-coupled microplate spectrophotometric assay was used to measure rates of ATP hydrolysis [57, 58] by *E. coli* DnaB and the influence on the rate by various constructs of λP and mutations (R403A-E404A-G406A) in DnaB.

In all experiments, DnaB was kept fixed at a concentration of 100 nM. To assess the contribution of unrelated helicases that may have co-purified with the various DnaB entities, we carried out control experiments with a bacterial protein extract prepared using the exact set of steps described above for DnaB, except that the pET24 vector that was used did not include either the DnaB or λP genes.

NADH oxidation data were recorded in the presence of 2 mM ATP (GoldBio #A-081-100), 2mM phosphoenolpyruvic acid monopotassium salt (PEP), 0.01 U/μL lactate dehydrogenase (Sigma-Aldrich, L1254), 0.002 U/μL pyruvate kinase (Sigma-Aldrich, P7768],) and 0.3 mM NADH in the following buffer: 50 mM HEPES-KOH, pH=7.5, 150 mM potassium acetate, and 8 mM magnesium acetate, 5 mM BME, and 0.25 mg/mL bovine serum albumin (BSA, Fisher #BP9706100). The above components were combined, save for ATP, into wells of a Corning 96-well clear round bottom UV-transparent Microplate (p/n: 3788) and the plate was warmed to 37 °C for 5 minutes in a pre-warmed SpectraMax M5 plate reader (Molecular Devices). After the warming phase, endpoint readings were taken at 340 nm wavelength to enable the pathlength to be measured. This was followed by quick addition of 2 mM ATP, mixing by pipetting action, and immediate re-insertion of the plate into the plate reader; absorbance data was taken at 340 nm every 30 seconds over a period of 30 min. Each experiment was performed in triplicate. Raw data was imported into Microsoft Excel for analysis. Each absorbance curve was manually inspected to identify the period during the experiment wherein the slope of the 340 nm absorbance vs time(s) was constant; in all cases this period was the complete 30 min period. The values in the above

time periods were divided by the 6,220 M^{-1} cm^{-1} extinction coefficient of NADH and the pathlength in cm calculated by the plate reader to produce the rate of ATP hydrolysis in M/s. After conversion to M/min, further division by the mg of DnaB in the assay provided the specific activity in M/min/mg.

Sample Preparation for Single Particle Cryogenic Electron Microscopy

BP complex in 20 mM HEPES-NaOH pH 7.5, 450 mM NaCl, 2 mM DTT, 0.5 mM $MgCl_2$, 0.2 mM ATP, and 5% glycerol (v/v) was diluted in glycerol-free buffer until the glycerol concentration was ~0.25%. Synthetic single-stranded DNA oligonucleotide 5'-TGACGAATAATCTTTTCTTTTTTCTTTTGTAATAGTGTCTTTT-3' [53] was resuspended in milli-Q water. To prepare complexes for cryo-EM, protein (1.5 μM) and DNA (1.875 μM) was mixed in a 1.25 molar excess. Protein-DNA complexes were applied to ultra-gold foil grids with holey gold support and 300 mesh size (R 0.6/1, Quantifoil Micro Tools GmbH); grids were flash-frozen as described [40] and were stored in liquid nitrogen until use.

Cryogenic-Electron Microscopy (Cryo-EM) Data Acquisition

A total of 25,959 un-tilted movies were recorded from the BP-ssDNA complex during a 96-hour Krios session involving Titan Krios1 (FEI, Hillsboro, Oregon), fitted with a Gatan K3 Summit (Gatan, Pleasanton, California) direct electron detector, operating at an accelerating voltage of 300 kV; the collection was managed by Leginon [59]. Single particle movies were collected at a pixel size of 1.083 Å, at a defocus range of -1 μm to -2.5 μm, at a dose rate of 25.51 $e^-/Å^2/s$ with a total exposure of 2 seconds for an accumulated dose of 51.01 $e^-/Å^2$. Intermediate frames were recorded every 0.05 seconds for a total of 40 frames per

movie. Additionally, a 25° tilted data set was collected from the same grid to mitigate expected preferred specimen orientation in the BP-ssDNA complex [60]; the tilted data set was measured similar imaging parameters as with the un-tilted collection.

Cryo-EM Image Processing

To enable computational handling, the 25,959 movies were divided into 4 groups, termed A, B, C, and D; identical computational procedures were applied to each group (Supplementary Figure 3S, 4S and Supplementary Table 3). The frames were aligned using motion correction and a B-factor of -500 Å², followed by the estimation of the Contrast Transfer Function (CTF) using the CTF fitting tool in WARP [61]. The WARP program was also used to extract approximately 12 million particles from 25,959 frames using the BoxNet2Mask_20180918 deep convolutional neural network and the following parameters: diameter = 150 Å, box size = 320 pixels, pixel size = 1.083 Å, dose per frame = accumulated dose of 51.01 $e^-/Å^2$ / 40 frames = 1.28 $e^-/Å^2$ / frame. The WARP extracted particles were imported into cryoSPARC v.3.3.2 [62–64], submitted to 2D classification and *ab-initio* reconstruction with C1 symmetry enforced. Each reconstruction produced 4 classes A0 to A3 (~360K, ~360K, ~790K, ~480K); B0 to B3 (~200K, ~160K, ~320K, ~170K); C0 to C3 (~370K, ~720K, ~490K, ~310K), D0 to D3 (~380K, ~600K, ~330K, ~330K particles). Inspection of these 12 classes for high-resolution features and numbers of particles suggested that the A2, B2, and C1 classes, which included 1.83 million particles (~790K, ~320K, and ~720K particles, respectively), be moved ahead to template-based heterogeneous refinement. As well, the class C3 volume, which did not resemble the BP complex, was also

included in the heterogeneous refinement procedure to exclude low quality particles. Template-based heterogeneous refinement was carried out with the published 4.1 Å EM density map (EMD-7076) [40] as the template. To avoid a calculation with 3 closely resembling volumes, we excluded the C1 volume owing to similarity to the volumes in classes A2 and B2. The heterogeneous refinement step produced 4 classes termed: E0, E1, E2, and E3. Class E0 (Supplementary Figure 3S, red volume) which featured the largest number of particles (~1.13 million) and provided the highest resolution map (4.41 Å), was carried forward to homogeneous refinement and non-uniform refinement. These procedures yielded EM maps with resolutions of 2.88 Å (Volume J, green in Supplementary Figure 3S) and 2.84 Å (Volume K, purple in Supplementary Figure 3S) respectively; the 2.84 Å map was judged to be of higher overall quality. Inspection of both maps after sharpening with DeepEMhancer [65] upheld this judgement. The 2.84 Å EM sharpened map, (Volume M, cyan in Supplementary Figure 3S) represented our highest quality map and was carried forward to model building (below).

Although the map derived from the E1 class (Figure Supplementary 3S, yellow volume) produced a map with similar resolution (4.41 Å) to that from the E0 class, we recovered a smaller number (~432K) of particles. Nevertheless, we submitted this class to homogeneous refinement and obtained a map with a resolution of 3.62 Å (Volume L, magenta in Supplementary Figure 3S). Model building into this map revealed a BP complex that lacked density corresponding to λP chain Z domain II. Classes E2 (Supplementary Figure 3S, gray volume) and E3 (Supplementary Figure 3S, orange volume) harbored ~100K particles each, at

9 Å and 8.55 Å, respectively. The low quality of all these maps precluded meaningful analysis.

To evaluate potential biases in the above procedure, the A2, B2, and C1 classes, the corresponding volumes, and the C3 class volume (from above) were also submitted to heterogeneous refinement, but, in this case, without a template. This procedure generated 4 classes (F0, F1, F2, and F3). We elected to move ahead with the F0 class because it featured the highest resolution (4.41 Å) map and the largest number of particles (~1 million); homogenous refinement of this class produced a map with a resolution of 2.95 Å (Volume G in Supplementary Figure 3S). A second effort encompassed classes F0, F1 (~380K particles), and F2 (~260K particles), which featured volumes with resolutions of 4.41 Å (above), 4.41 Å, and 4.50 Å (the F3 class produced a volume with a resolution of ~9 Å; the ~110K particles in this class were not pursued in this study). The combined set of particles from the F0, F1, and F2 classes (1.7 million particles) was submitted to a second round of heterogenous refinement. This procedure produced 4 classes (H0, H1, H2, and H3). The highest resolution volume (4.41 Å) and the largest number of particles (~1 million) were recovered in class H0. Homogeneous refinement of these particles provided a 2.93 Å map (Volume I in Supplementary Figure 3S). The 2.95 Å and 2.93 Å maps obtained from the non-template approach did not provide maps that exceeded the quality that we had already obtained when a template was used in refinement. Classes H1, H2, and H3 harbored smaller numbers of particles, ~270K, ~220K, and ~175K, respectively, and produced maps with resolutions 4.41 Å, 4.41 Å, and 6.74 Å, respectively. These maps, even after

sharpening, did not reveal information not already seen in the high quality 2.84 Å EM map described above.

The four classes recovered above from group D (D0, D1, D2, and D3) were submitted to heterogenous refinement to yield four classes (N0, N1, N2, and N3). The N1 class, with the highest resolution volume (4.41 Å) and largest number of particles (~860K), was moved forward; the other classes N0 (~6 Å with ~320K), N2, and N3 (both at ~8 Å with ~230K) particles were abandoned, since they produced volumes with no resemblance to the BP complex. Homogenous refinement, a second round of 2D classification, *ab initio* modeling, and heterogeneous refinement, applied to class N1, produced four classes (O0, O1, O2, and O3). The O2 class, with the highest resolution map (3.92 Å) and the largest number of particles (~450K) surpassed what we recovered in classes O0, O1, and O3 at <4.1 Å, with ~100K particles, each. Consequently, O2 advanced to the next stage in the refinement step. To explore whether the O2 class would produce a higher quality reconstruction, we combined the particles in O2 with those in the K, G, and I to obtain 3.7 million particles; CryoSPARC culled duplicate particles to yield a set with 1.7 million particles. This particle set underwent *ab-initio* reconstruction, heterogeneous refinement, homogeneous refinement, and non-uniform refinements. Homogeneous and non-uniform refinement procedures produced two maps, each with a resolution of 2.81 Å (Volumes P and Q in Supplementary Figure 3S). Notwithstanding the resolution, the quality of these density maps was substantially lower than the ones described above.

The tilted dataset was processed in the same manner as described above and produced a final map with a resolution of 3.30 Å. Combination of this map with the 2.84 Å described above did not improve on the original map. Owing to its overall lower resolution, the tilted data set was not pursued further.

Model Building and Refinement

The published BP model (PDB: 6BBM) was positioned in the 2.84 Å EM-map using the MolRep program [66–69]. Five copies of the 1.86 Å λP domain III could also be reliably positioned in the EM map. We calculated the complete model of λP with the Google CoLab implementation of AlphaFold in ChimeraX: [46, 47, 70]. Density corresponding to the amino-terminal domains I/II (1:118) of one copy of λP, which had been poorly resolved in our earlier study [40], was sufficiently ordered to allow fitting of the amino-terminal alpha helical domains I/II of the AlphaFold calculated structure for λP chain Z. AlphaFold predicted Domain I to be a straight helix, however, this conformation did not comport with our EM map, and hence the helix had to be bent after Glu-14. Our maps also showed features that may correspond to one additional amino-terminal domain (Chain Y); however, this density could not be interpreted.

To build a model of the BP complex for refinement, we leveraged availability of high-resolution crystal structures of the amino-terminal domain of DnaB• (PDB: 1B79, 2.3-Å [71]), domain III of the λP (1.86 Å, this work), as well as Alphafold models of both *E. coli* DnaB and λP [46, 47]. These components were combined by superposition onto an earlier BP structure to provide a model with excellent starting stereochemistry. Portions of the DnaB and λP that could not be positioned by superposition (DnaB residues: 25:30, 166:181, 500:501, and λP residues: 1:23,

78:82, 99:100, 120:122, 186:212, 226:232) were built by hand in COOT using the Alphafold model as a guide. We reasoned that a model built in this way would perform best in a restrained real space refinement against our 2.84 Å cryo-EM map in Phenix [51].

Model refinement was performed in Phenix against the 2.84 Å. DeepEMhancer enhanced map utilizing the rigid body, minimization global, NQH flips, and the atomic displacement parameters (adp) calculations in its real space refinement function; refinement also employed Ramachandran and secondary structure restraints (the same entries for each DnaB and λP chain) and the following rigid bodies (DnaB residues: 1:173, 174:200, 201:468; λP residues: 1:118, 119:192, 193:233). The final model encompassed the following DnaB residues (chain A: 25:173 and 201:468, chain B: 16:468, chain C: 19:468, chain D: 18:468, chain E: 19-468, and chain F: 24:468) and λP residues (chain V: 119:232, chain W: 119:232, chain X: 119:232, chain Y: 119:232, and chain Z-2:231). Our model also included 5 ADP molecules bound to 5 magnesium ions in each of the five DnaB chains: A, C, D, E, and F; chain B lacked any nucleotide (Supplementary Table 3).

Model Analysis and Visualization

Structural analysis and visualization of the DnaB – λP complex were carried out using the CCP4 software package [69], Coot [72, 73], the Uppsala software suite [74–77], UCSF-CHIMERA [70], Phenix [51, 78–84], PyMOL [85], and as described previously [40]. Distances and angles within and between protein structures were calculated using the PyMol Python scripts titled “pairwise_dist”

(https://pymolwiki.org/index.php/Pairwise_distances) and "angle_between_domains" (https://pymolwiki.org/index.php/Angle_between_domains). Molecular graphics and figures were generated using UCSF-CHIMERA [70] and PYMOL [85]. Software used in this study was sourced from the SBGrid Consortium [86].

Results

Complete Structure of the λP Helicase Loader

To improve upon our prior analysis of the BP complex [40], we applied protein engineering, experimental structural analysis, and AlphaFold structure prediction [46, 47] to define the complete structure of λP. Using the structure of λP within the BP complex (PDB = 6BBM, [40]) as a guide, we isolated a soluble fragment of λP (residues 105 to 210) and determined its X-ray crystal structure (residues 119 to 192) at 1.86 Å (Figure 1 and Supplementary Table 2). The resulting structure revealed a three-helical structure resembling that seen in the earlier cryo-EM analysis; further the crystal structure confirmed prior inferences about λP's protein chain direction and the approximate side chain mappings to the structure.

The AlphaFold calculation provided five predicted conformers of λP; each conformer harbored four domains: two compact domains (domain II: residues ~30 to ~119; domain III: residues ~120 to ~192) and two flexibly linked structural domains at the amino (residues 1 to ~29) and carboxy (193 to 233) termini with a single alpha helix, termed the N-terminal and C-terminal lasso/grappling hooks (Figure 1). The crystal structure of λP domain III superimposed well on the

AlphaFold predicted structure (root mean square deviation (RMSD) of 0.328 Å over 478 atoms). AlphaFold predicted a four helical bundle for the amino terminal domain (domain I/II) that terminated in a lasso-like amino-terminal helix. Notably, the diverse configuration of the AlphaFold predicted conformers hint at flexibility in the arrangement of the four domains.

The 2.84 Å Cryo-EM Structure of the *E. coli* DnaB – λP Helicase Loader

The goal of this work had been to obtain a cryo-EM [87–90] structure of the BP complex bound to ssDNA. Although the results of native mass spectrometry analysis revealed the clear presence of a BP-ssDNA species [40] and described below, the 2.84 Å map that we obtained did not reveal the position of the ssDNA. Although devoid of ssDNA, our EM maps were of higher resolution than our prior study [40] and revealed the complete structure of one of the five copies of the λP loader (Figure 2, chain Z); the carboxy-terminal domains of the other four protomers were also seen. The higher resolution structure also clarified the interface between helicase and loader, as it amplified findings about the right-handed open spiral configuration of the DnaB helicase [40, 45]. The crystal structure of λP domain III could be unambiguously positioned into each copy of the loader in our map. In the 2.84 Å BP complex (Figure 2), five domains III/IV of the λP loader ensemble bind at DnaB subunit interfaces; notably, the C-terminal helix of each monomer, now termed the C-terminal lasso/grappling hook, binds DnaB at a site formed out of the DH and LH elements. Density corresponding to the amino-terminal domains I/II (residues 1-119) of one copy of λP (chain Z), which had been poorly resolved in our earlier study [40], was sufficiently ordered to allow fitting of the model calculated by AlphaFold. Our map also showed features that

may correspond to one additional amino-terminal domain belonging to λP chain Y. No density was observed for the amino-terminal domains of λP chains V, W, and X; as such, our work is silent on these elements. Notably, the configuration of the four λP domains in the AlphaFold-calculated structures did not match that seen in our EM maps, as such, considerable adjustment of the calculated structure was required for fitting into our map.

As with our prior analysis [40], the BP complex presents as a three-tier entity with its λP and DnaB components arranged in a right-handed open spiral configuration, however, the higher resolution (Supplementary Figures 3S, 4S, and Supplementary Table 3) of the current model enables a deeper and more complete analysis. The five copies of the λP loader primarily bind on the CTD side of DnaB, tracing out a spiral that is congruent with spirals traced out by the CTD and NTD tiers (described below). We find no buried surface area and, correspondingly, no contacts between the five copies of λP in the loader complex; it remains possible that contacts may exist between the four invisible amino terminal domains of λP (chains V, W, X, and Y). An overall conclusion from this finding is that the five λP monomers bind to DnaB independently.

In comparison to the closed planar constricted form of DnaB, both the CTD and NTD layers of the DnaB hexamer in the 2.84 Å model of the BP complex feature a similar configuration to that seen in the earlier analysis, with similar average helical pitch (17.4 Å), rise (4.5 Å), and twist (56.4°) parameters for the CTD tiers. As well, the NTD and CTD sub-domains bury similar amounts of surface area (BSA) at their respective interfaces (NTD-head-to-head: ~690 $Å^2$; NTD-tail-

to-tail: ~1950 Å; CTD: ~2100 Å^2, excluding the breached interface). Distortions in the DnaB hexamer that accompany transition from the closed planar (Stage I) to the right-handed open spiral breach one of the six interfaces (Stage II), on both the NTD and CTD tiers, create openings of appropriate size (NTD: ~8.5 Å; CTD: ~9.5 Å) to admit ssDNA (width: ~7.5 Å) into the inner chamber.

The λP loader ensemble grips the DnaB helicase at five discrete and widely dispersed sites; each of these sites are DnaB-specific insertions into the recA-fold (Supplementary Figure 5S). Owing to the asymmetry of the complex, not every λP instance uses every site (Figure 3). The five sites on DnaB are: 1) the DH element (residues 291:307) on chain B of the breached interface (its partner LH element from chain A is not visible in our maps); the N-terminal lasso of chain Z is the only λP element to make this contact (BSA: ~1980 Å^2). This contact partially explains the finding that deletion of λP residues 9:85 disrupts the BP complex [91]. 2) A short DnaB helix comprised of residues 387:391 on the CTD at the breached interface; this contact is only made by domain II of λP chain Z (BSA: ~325 Å^2). 3) A wide patch that spans two adjacent DnaB CTDs (residues 424:434, 456 on one CTD and residues 391:395, 429:430, 446:449 and 468 from the adjacent CTD) and includes contacts (residues 447:450) on the arginine finger-beta-hairpin of each CTD; domain III of each λP monomer contacts this patch (BSA: ~1660 Å^2). 4) a site comprised of the DH (residues 290:307) and LH (residues 182:199) elements of two adjacent DnaB subunits; the C-terminal lasso of each λP monomer makes this contact (BSA: ~1380 Å^2). Notably, the nature of the DnaB•λP interfaces at sites 1 (λP N-terminal lasso) and 4 (λP C-terminal lasso), both of which include

DnaB DH elements, diverge considerably; indeed, the N-terminal lasso occupies the same space as that of the chain B LH element (Figure 4 and Supplementary Figure 8S). 5) A patch on the NTD of DnaB (residues 76:77, 183:195); two λP's (chain Y and chain W) make this contact (BSA: ~400 $Å^2$). Our structure provides a partial rationale for the finding that certain DnaB mutants (residues V256I/E426K and G338E/E426K [91]) exhibit resistance to inhibition by λP since residue 426 is found at interfacial site #3. Residues 256 and 338 are packed against one another in the CTD but are distant from the BP interface; we speculate that mutations at these sites disrupt the structure of the CTD.

The extensive interface between the λP ensemble and DnaB stands in contrast to the considerably more modest interface formed by the DnaC loader assembly [40, 41, 45]. The six N-terminal lassos/grappling hooks of DnaC make essentially identical interactions with DH-LH interface of each DnaB subunit; this binding site overlaps with site #4 of the BP complex. Unlike domain III of λP, which slightly overlaps with the position of the AAA ATPase domains of DnaC, the latter domain makes no contact with DnaB.

To gain additional insights into the widely dispersed sites of interaction between DnaB and λP, we performed a series of binding and ATPase studies with truncated constructs of the loader (Figures 3B and Supplementary Figures 6S and 7S). This study leveraged constructs that encompassed λP domains I (residues 1:30), I/II (residues 1:98, residues 1:105), III and part of IV (residues 105:210), III/IV (residues 110:233), and IV (residues 191:233, residues 210:233). In prior work, we had demonstrated, using co-expression, that the carboxy terminal

domains III/IV (residues 102:233) binds to DnaB [40] and, here, we show a capacity to suppress DnaB's ATPase activity. Using so-termed NiNTA 'pull-down' experiments, we also observe robust binding to closed planar DnaB by domain IV. However, both isolated domain I (residues 1:30) and domain I/II (residues 1:98) fail to exhibit binding in our assay. Domain I/II (residues 1:105) and domain III with part of IV (residues 105:210) both showed weak binding to closed planar DnaB. Our data suggest that λP domain IV retains most of the binding energy. Parallel ATPase rate measurements align with these findings; only when λP domains III/IV (residues 102:233) is co-expressed with DnaB do we find suppression of DnaB's activity; inclusion of all other λP truncations (purified separately and combined with DnaB *in vitro*) reveals near wild-type ATPase activity (Supplementary Figures 6S and 7S).

Taken together, our structural, genetic, and biochemical analyses provide a more complete perspective on the *E. coli* DnaB - λP complex and establish a foundation for interrogating its further assembly into the initiator-origin complex.

The Amino-Terminal Domains (I/II) of One Copy of the λP Loader Seals DnaB's Internal Chamber

Two aspects of finding the complete structure of one of the five λP loaders are remarkable (Figure 4). First, we observe that the complete structure of λP chain Z, through its contacts to DnaB subunits A and B (and F), spans the breach in the open spiral. Specifically, we find the uniquely ordered domains I and II of chain Z positioned at the top of the DnaB spiral (in the pose of Figure 2); this arrangement precludes entry of a physiological origin-derived ssDNA into the central chamber. As such, even though openings in the NTD and CTD tiers of

DnaB provide entrances for ssDNA of sufficient size, disposition of chain Z effectively seals entry into DnaB's inner chamber to a physiological ssDNA bubble-shaped substrate at a replication origin (Figure 4). Second, it is now clear that the five subunit λP ensemble will be radically asymmetric. The presence of a single breach in DnaB implies that only one copy of the λP ensemble can populate the configuration adopted by chain Z; the remaining protomers must necessarily feature different configurations and play distinct roles during replication initiation, for example, contacts to the λO initiator protein. Notably, these two features distinguish the λP and DnaC ensembles [40, 41, 45]; the DnaC ensemble neither impedes entry of ssDNA into the inner motor chamber, nor is it asymmetric.

Comparison of the higher resolution BP model with the BC complex [40, 41, 45] reveals an additional surprise: the N-terminal lasso/grappling hook of λP-chain Z positions the N-terminal helix of this element against the DH helix of DnaB chain B; this position overlaps with the lasso/grappling hook of DnaC which is bound at the same site (Figures 4C and Supplementary Figure 8S). Notably, although the binding modes of λP's five C-terminal lassos are identical and resemble those of DnaC, save for the change in protein chain direction, the N-terminal lasso binds to the DH helix via a binding mode that differs from that seen with the C-terminal lasso (Supplementary Figure 8S). Interestingly, one λP protomer (chain Z) binds at the top and bottom of the breach (in the pose in Figure 2), using the N-terminal and C-terminal lassos, respectively. However, in the DnaC complex, these functions are carried out by two distinct protomers, chain G and chain L at the top and bottom of the spiral. For both loaders, positioning of cognate elements on

DnaB chain B at the top of the spiral could sterically suppress closure of the helicase. This finding represents another example wherein the unrelated λP and DnaC helicase loaders have evolved to converge on the same solution: positioning of a loader helix in a similar, but distinct, binding mode on the DH element at the top of the DnaB spiral. In this context, it is noteworthy that λP's higher affinity to DnaB, which can displace DnaC from the BC complex [92], may be explained by the multitude of contacts to DnaB made by the λP ensemble, and especially chain Z.

Taken together, the 2.84 Å structure of the *E. coli* DnaB - λP complex forces reconsideration of the mechanism of helicase loading. The finding that one completely ordered λP protomer binds across the DnaB breach and blocks access of ssDNA to the inner chamber implies a previously unrecognized autoinhibited configuration. Our work predicts that remodeling of the BP complex to clear the path for ssDNA into the DnaB hexamer must accompany recruitment of the BP complex to the replication origin. In addition, the λP ensemble features an asymmetric configuration with one protomer binding at the DnaB breach and the remaining protomers implementing yet to be described mechanisms. Further, the unique features of the λP ensemble distinguishes it from the DnaC loader and suggests that overlapping, and distinct, mechanisms might be implemented by each loader.

The Carboxy-Terminal Lasso of the λP Ensemble Shears the LH-DH Interface of Each DnaB Monomer

During transition from the closed planar to the open spiral forms, each C-terminal lasso helix of the λP ensemble binds alongside 5 DH - LH elements to

create a three-helical bundle (sites #4 and #5); binding shears and nearly completely disrupts the underlying DH-LH interface (Figures 3 and 5). Notably, both the DH and LH elements are unique to the DnaB family of helicases in comparison to other recA family members ([93], Supplementary Figure 5S). As noted above, the N-terminal lasso of λP binds to the sixth DH element (chain B) in DnaB (top of spiral as in the pose in Figure 2); this DH element lines the breach in the hexamer (site #1). Binding wholly expels the partner LH element (chain A) since the N-terminal lasso-helix takes its place; indeed, the sixth, chain A, LH helix is not seen in our EM maps.

In the closed planar form, the DH element of each DnaB subunit packs against the LH element of an adjacent monomer in an antiparallel fashion via an interface whose Cα atoms are, on average ~15.2 Å apart (4NMN (constricted): 14.7 Å, 2R6D (dilated): 15.4 Å, 3BGW (constricted): 15.5 Å). In closed planar *E. coli* DnaB (modeled on the 4NMN structure [24]), the underlying contacts between the DH and LH elements are mediated by primarily hydrophobic interactions (Figure 5). For example, DH residue Trp 294 packs into a pocket formed by LH residues Val 190, Ile 193, and Phe 197 on an adjacent DnaB subunit. DH residue Met 301 packs in a pocket comprised of LH residues Leu186 and Val 190; DH residue Leu 305 binds in a pocket lined by Ala 183 and Leu 186.

Our prior work had shown that the DH-LH interfaces in both the BC [41] and the BP complexes [45] are disrupted by the DnaC and λP loaders. In the 2.84 Å BP structure, we observe that the helical segment (residues 211:227) of each C-terminal lasso of λP is positioned alongside the DH-LH elements. In comparison

to the closed planar form, the DH and LH helices are rotated by ~+8° and ~-8°, respectively, and translated 2-5 Å away from each other. Collectively, these changes increase Cα distances between the DH and LH elements by ~2 Å from ~15.2 Å in the closed planar form to ~17.2 Å in the λP-induced open spiral. An important overall consequence of λP binding is the near complete abrogation of interactions between the DH and LH elements in the DnaB open spiral (Figure 5). The repositioned DH and LH elements combine, separately, with the λP C-terminal lasso helix to produce a three-helix assembly; the disrupted DH-LH interface is replaced with distinct contacts between each element and residues in λP C-terminal lasso helix. In the repositioned DH element, DnaB Trp 294 packs against λP residues Lys218 and Ile219; DH residue Met 301 resides next to λP residues Ile 222 and Phe 226; DH residue Leu 305 contacts λP residue 226 as it maintains contacts with LH residue Ala183 (the sole contact between DH and LH in the loader complex). As well, the repositioned DnaB LH elements contacts the λP C-terminal lasso helix. LH residue Glu 194 contacts Ile 219. Notably, the DH-LH-λP three-helix bundle interaction is identical in all five instances of B_2P_1 in the BP complex as indicated by superposition (root mean square deviations of 0.61 to 0.67 Å on 246 Cα atoms (Supplementary Figure 9S). We found that, although not included in the superposition, the second CTD DnaB in the B_2P_1 sub-structure and domain III/IV of the λP superimpose well; this suggests that a relatively rigid DnaB-CTD_2-λP substructure.

Unlike four λP protomers (chains, V, W, X, and Y), which contact two DnaB subunits, chain Z contacts three DnaB chains (B, A, and F). The interaction with

chain B at the top of the spiral (as in the pose in Figure 2) is mediated by the N-terminal lasso helix of λP which is positioned adjacent to the DH element that lines the breach in the hexamer. In contrast to the three-helical DH-LH-λP bundle seen with the five instances of the B_2P_1 sub-structure, a two helical bundle is observed (Figure 2 and Supplementary Figure 8S). In this species, the LH element (chain A) has been displaced and is not visible in our maps; in its place, we find the λP N-terminal lasso helix. Notably, the same DnaB (chain B) DH residues highlighted above (Trp 294, Ile 297, Met 301, and Leu 305) participate in the divergent interaction with the N-terminal lasso helix of λP. DnaB DH residue Trp 294 contacts λP residue Met 16; DnaB residue Ile 297 packs against Gln 15; DnaB residue Met 301 packs into a pocket formed out of λP residues Phe 11, Asp 12, and Met 8. Finally, DnaB residue Leu 305 is found in a pocket comprised of Met 8 and Val 9. The resolution of our maps is relatively low in the volume encompassed by site #1, as such, description of the underlying interface should be considered tentative.

Examination of the configuration of various DnaB structures suggests that the DH-LH interface is an important nexus of structural changes during the helicase loading. (Importantly, the moderate resolution (2.8 – 3.8 Å) of the available structures constrains our analysis.) Measurements of the distances between DH and LH elements in the closed planar forms of Stage I (dilated: 2R6D [25] and constricted: 3BGW [23] and 4NMN [24]) reveals a ~15.2 Å separation. In the Stage II DnaC loader bound conformers, with and without ssDNA, the distance between DH and LH elements increases to ~17.5 Å; this value follows closely the

~17.2 Å distance seen in the 2.84 Å BP complex structure. With the expulsion of the loader and transition to the translocating Stage IV, the DH and LH elements move closer together (4ESV [26]: 15.5 Å, 7T20:16 Å [94], 7T21:16.06 Å [95], 7T22: 16.1 Å [96], and 7T23: 16.20 Å [97]), but perhaps, not as close as the Stage I structures. Notably, in *V. cholerae* (VC), isolated (PDB: 6T66, [98]) and DciA bound DnaB (PDB: 8A3V, [18]) diverge from the above trends. The average DH – LH distance in isolated closed planar VC DnaB is ~17 Å, which is close to values extracted from loader bound open spiral forms of DnaB. Furthermore, this distance appears to contract (15.6 Å) in the DciA bound closed planar form of DnaB. Divergences in distances between DH – LH elements may suggest substantially different loader mechanisms between the DnaC/λP and the DciA helicase loading systems.

Our work establishes the helical DH – LH DnaB elements as important moving parts in the loading pathway. Binding of the λP loader disrupts the hydrophobic packing seen the DH – LH element of the closed planar configuration to yield two new interfaces between the same surfaces of each element and the C-terminal lasso; a distinct interaction is seen between the DH elements and the λP N-terminal lasso.

The λP Ensemble Binds to and Stabilizes the DnaB Spiral

The right-handed open DnaB spiral found in the λP loader complex is stabilized by an extensive interface between helicase and loader (Figures 2, 3, and 6). Domain III of each λP loader integrates hydrogen bonds, electrostatic van der Waals, hydrophobic and electrostatic interactions to contact two consecutive DnaB subunits (interaction sites #2 and # 3 above). For example, λP residues 145:162

contact a DnaB loop (residues 424-429) on one subunit, while λP residues 131:141 and 169:174 of the same chain contact a DnaB loop (residues: 391-398) and a strand (residues: 447:449) on a neighboring subunit. Moreover, as noted above, the structural correspondence between the 5 instances of the DnaB-CTD_2-λP sub-structure points to nearly identical interfaces, at the current resolution, between subunits of DnaB and λP in the complex.

Although the DnaC and λP loaders are unrelated in structure, the DnaB portion of the BC [41] and BP [40] complexes adopt very similar right-handed open spiral configurations [45], however, the underlying arrangement of the CTDs is not identical; this divergence is reflected in the distinct helical parameters of each CTD spiral (BP: average helical pitch (17.4 Å), rise (4.5 Å), and twist (56.4°); BC: average helical pitch (19.3 Å), rise (5.5 Å), and twist (55.3°). This distinct architecture arises from wedging apart of the two CTDs in each B_2P_1 sub-structure by 2.5° relative to the arrangement seen in the BC complex; this translates into 1-2 Å shifts in CTD positions (Figure 6). Disposition of DnaB subunits in the BP complex is a direct consequence of the unique interface made with λP. The pentameric λP ensemble features an extensive interface with the helicase, and it is the contacts mediated by λP domain III that mediate wedging apart of DnaB subunits. On the other hand, the globular domains of the hexameric AAA+ DnaC ensemble, make no contacts with DnaB whatsoever; absence of contacts permits closer approach of individual DnaB subunits to each other than is possible in the BP ensemble.

The observation of similar helicase configurations in the BP and BC complexes led us to previously suggest that the open spiral might be an intrinsic DnaB state since it is observed in complexes with a loader that forms an extensive interface (λP) and one that does not (DnaC) [40, 41, 45]. The 2.84 Å BP complex structure teaches that the open spiral configuration may well be intrinsic, however, the interaction with λP also drives changes in the spiral that are not seen when DnaC binds to DnaB. Whatever the source, an overall consequence of the inability of DnaB subunits in the BP or BC complexes to approach each other optimally has profound consequences for both ATP hydrolysis and ssDNA binding.

Nucleotide Hydrolysis by DnaB is Directly Suppressed by λP

Although the BP sample submitted to cryo-EM analysis was supplemented with an excess of ATP (0.2 mM), 5 of 6 sites on DnaB in the complex harbored density that could only be modeled with ADP (Figure 7); the nucleotide site on the subunit that lines the breach (chain B) was found to be unfilled. In the sites filled with ADP, in addition to a pocket formed out of the conserved GKT (residues 236-238) Walker A and Walker B (residue D343) motifs, DnaB residues Gln281, Thr282, and Arg285 surround the 6 amino group of the adenine group, with the potential to form weak hydrogen bonds (~3.8 Å), however, essentially all these interactions could also be made by the 6 oxo group of guanine; the smaller pyrimidine bases could not form these interactions. There are no contacts to the ribose sugar. As such, lack of specificity for ribonucleotide bases revealed by solution studies, including the lower affinity for purine ribonucleotides [99], is represented in our structure.

The open spiral configuration of DnaB in the BP complex rearranges the composite ATP sites into configurations ill-suited for hydrolysis and/or ADP release (Figure 7). ATP binding and hydrolysis on DnaB take place at composite sites with structural elements that span two subunits; the Walker A/P-loop and Walker B elements are found on one subunit and the beta-hairpin arginine finger, which completes the site, resides on an adjacent subunit [10]. Prior work ([92] and Supplementary Figures 6S, 7S. and 10S) found that DnaB's ATPase activity is fully suppressed in the BP complex. Each nucleotide binding site in the structure of the BP complex is disrupted relative to the presumed active configuration in the translocating form (PDB: 4ESV, [26]). Inspection of the B_2P_1 superposition described above suggests that relative to the translocating form, the CTDs of DnaB are rotated outward away from the central chamber by 16-19° (Figure 7). Changes in CTD configurations between loader bound and translocating DnaB result in ~2-4 Å shifts in the beta-hairpin arginine finger sub-structure; Lys 418 and Arg 420, both implicated in ATP hydrolysis in DnaB family members [100, 101], are found shifted by ~2 Å in the loader-bound form.

Outward rotation of the CTDs is directly linked to loader binding since domain III of λP makes contacts with two adjacent DnaB CTDs, including the arginine finger-beta-hairpin of each CTD (site #3), as noted above (Figure 7). Close inspection of the superposition shows that the position of λP-domain III is incompatible with the position of the DnaB CTDs in the translocating form. As such, the λP loader stabilizes a DnaB configuration that precludes the formation of nucleotide binding sites competent for hydrolysis and/or ADP release, and thus,

neatly accounts for the ATPase biochemical data ([92], Supplementary Figures 6S, 7S, and 10S). Support for the idea that suppression of ATPase activity arises from shifts in the hairpin, and the direct role played by λP in specifying the shift, is supported by comparisons with the analogous BC complex, which also lacks ATPase activity. The architecture of the ATP sites in the BC complex resembles those seen in the BP complex, although positional shifts in the arginine-beta hairpin are not as extensive (Figure 7). DnaC, which is unrelated in structure to λP, adopts a distinct architecture when bound to DnaB that completely lacks contacts to the arginine-finger hairpin; absence of these contacts may explain the smaller shift of the hairpin in the BC complex.

For the reasons presented above, we conclude that surfaces from domain III of λP promote and stabilize the shifted configuration of the hairpin, and concomitantly, contribute to suppression of ATP hydrolytic activity.

Does the BP Complex Bind ssDNA Outside of the Central Chamber?

The shape and geometry of the ssDNA binding site in the central chamber of DnaB differs significantly between the λP loader-bound (State II, [40]) and translocating states (State IV, PDB: 4ESV, [26]). In the translocating form, each DnaB subunit projects a DNA binding loop into the central chamber to provide contacts by three residues (*G.st*: R381, E382, G384; *E. coli*: R403, E404, G406) per subunit to ssDNA. The pitch of the closed DnaB spiral is a close match to the pitch of the ssDNA spiral providing for equivalent contacts between each helicase subunit and the nucleic acid backbone. However, the pitch and twist of the closed spiral DnaB (PDB: 4ESV, ~7.5 Å, ~60°) differs significantly from values (~4.5 Å, 56.4°) observed in the BP complex. Divergently configured DnaB spirals critically

displace the positions of ssDNA binding residues in the loader complex between 2.7 Å – 19.5 Å (A: 5.5 Å; B: 2.7 Å; C: 4.5 Å; D: 10.9 Å; E: 16.2 Å; F: 19.5 Å) from values in the translocating form. Notably, the positions of the ssDNA binding residues in the BC complex resemble those in the BP complex, though the deviations from the translocating form are not as great owing to distinct binding modes between the DnaC and λP loaders. Although the architecture of the ssDNA binding central chamber is altered in the BC and BP complexes and might preclude ssDNA binding, it is formally possible that binding may be mediated by a different mode.

Not only is the ssDNA binding site disrupted in the loader complex, but two other structural features of the BP complex sever access to the central chamber. First, as described above, one λP monomer (chain Z) binds to two DnaB subunits that span the breach, and in doing so, uses λP domains I/II to physically block entry of ssDNA into the chamber. Second, owing to contacts between λP domain III and DnaB, the central chamber is unable to achieve the active form while the loader remains bound (Figure 7). As noted above, for DnaB in the BP complex to achieve the configuration in the ssDNA complex, each CTD must rotate by 16-19° towards the central chamber. However, steric clash between each λP domain III and pairs of DnaB CTDs in the ssDNA complex would preclude this structural change. This finding stands in stark contrast to the BC complex where DnaC's divergent binding mode places no restriction on adoption by DnaB of the conformation in the ssDNA complex. Indeed, in the BC-ssDNA complex (PDB: 6QEM, [41]), DnaB adopts

configuration closely related to that in the ssDNA-bound translocating form (PDB: 4ESV, [26]).

Notwithstanding the distorted shape and geometry of its internal chamber, the BP complex is known to robustly bind ssDNA [40], furthermore, the λP loader is predicted to contact ssDNA [53]. To gain insights into the path of ssDNA through the BP complex, we prepared mutants of DnaB with the goal of separating contacts to ssDNA in the complex arising from DnaB or λP. By mutating the three DnaB residues (R403, E404, G406) per subunit that contact ssDNA to alanine, we reasoned that we could abolish ssDNA binding in the central chamber. We used native mass spectrometry (MS) to compare binding between wild-type BP, wild-type DnaB, and DnaB$^{R403A-E404A-G406A}$, wherein ssDNA-binding residues in each subunit were mutated (R403A, E404A, and G406A, total: 18 changes), to remove contacts seen in the ssDNA complex (Figure 8 and Supplementary Table 1). Our measurements confirmed robust binding by the BP complex of ssDNA. Measurements with wild-type DnaB showed robust binding, while ssDNA binding by DnaB$^{R403A-E404A-G406A}$ was diminished to ~25% of the wild-type value. Our efforts to measure ssDNA binding by the DnaB$^{R403A-\ E404A-G406A}$ – λP complex by native MS were stymied by poor solubility of the mutant complex upon buffer exchange into native MS solution. Parallel ATPase measurements (Supplementary Figure 10S) suggest that DnaB$^{R403A-E404A-G406A}$ retains the biochemical and λP binding properties of wild-type, suggesting no overall perturbation of its structure. DnaB$^{R403A-E404A-G406A}$ is also more active than wild-type (we do not know the reason

for the enhanced activity), and this activity is suppressed in the purified DnaB$^{R403A-E404A-G406A}$ – λP complex.

Failure to completely abolish ssDNA binding in DnaB$^{R403A-E404A-G406A}$ implies that additional contacts remain, perhaps, outside of its central chamber. These data raise several intriguing possibilities: 1) the λP loader, while bound to DnaB contributes most, if not all, of the significant contacts to ssDNA, and 2) ssDNA is bound by DnaB, but not in the central chamber, but on the outer surface of DnaB. Such a distinct ssDNA binding mode is hinted at by autoinhibited nature of the present complex and its distorted central chamber binding site. Of course, it is possible that the BP-DNA complex blends elements from both of the above. In support of the notion that DnaB leverages its outer surface in the initial ssDNA encounter complex, prior work by Trakselis and co-workers provides ample evidence for existence of contacts to ssDNA by the outer surface of DnaB [102, 103].

Taken together, our structural, genetic, and biochemical analyses imply a previously unrecognized intermediate in the helicase loading pathway wherein origin-derived ssDNA is bound by the BP complex but has not yet been admitted into the central chamber of DnaB, and that remodeling of the complex must precede deposition of ssDNA into the inner chamber in preparation for translocation.

Discussion

Our 2.84 Å structure of the *E. coli* DnaB – λP helicase loader complex provides new insights into structure, function, and assembly of the DnaB replicative

helicase at a bacterial origin. Our work reveals a previously unrecognized autoinhibited intermediate for ssDNA loading, as it highlights structural elements on DnaB that undergo conformation switching during helicase ring opening. We also provide evidence that physiological origin-derived ssDNA may initially contact the helicase•loader complex outside of the inner chamber of DnaB.

The 2.84 Å BP model revealed a radically asymmetric configuration for the λP ensemble. The C-terminal domains of four protomers (chains V, W, X, and Y) of λP are found in configurations closely related to those in our earlier structure [40]; the N-terminal domains of these chains remain poorly ordered. Notably, one λP monomer (chain Z) is fully ordered in our structure and found to span the breach in the DnaB open spiral. In addition to interactions made to adjacent DnaB subunits (chain A and F) by the C-terminal linker/lasso domain (III/IV), the N-terminal domain also contacts a third DnaB subunit (chain B) across the breached interface; this contact involves the N-terminal lasso element which packs against the DH helix at the breached interface. This novel asymmetric interaction could imply that λP (chain Z) is the first loader monomer to bind to DnaB and trigger transition to the open spiral, with the other chains playing secondary roles. Of course, chain Z's multivalent contacts could also serve to block reclosure of DnaB to the closed planar form. The finding that the λP loader harbors lasso elements at both the amino and carboxy termini creates a conceptual link with certain homologs of the DciA loader, which also feature similar architectures at both termini [7, 19]; however, a mechanistic relationship between λP and these DciA loaders remains to be established. The current BP structure suggests no

difference in configuration between the five instances of the λP lasso helix-DnaB-LH-DH-sub-structure, leaving unanswered questions of how breaching of the single cracked interface of DnaB is specified and/or what are the roles of the λP monomers that are not located at the breached interface.

Binding of the five lasso/grappling hooks of the λP ensemble to consecutive DH-LH junctions on DnaB has been suggested to trigger the change from the closed planar to the right-handed open-spiral form of DnaB [41, 45]. The five λP CTDs contribute to this mechanism by positioning five lasso/grappling helical elements (domain IV) at the DH-LH junctions; these interactions force the DH and LH helices to rotate by ~8° and translate by 2-3 Å away from each other. Reconfiguration brings the DH and LH elements into new interactions with the five lasso elements of the λP ensemble. Further, examination of the DH-LH distances amongst all the hexameric DnaB structures in the PDB implies roles for these elements in the helicase assembly pathway [23–26, 94–97]. Intriguingly, divergence in the pattern of distances between the DH and LH elements induced by λP/DnaC and the DciA systems [18, 98] hints at distinct helicase loading mechanisms that have yet to be clarified.

Although the two tiers of the open-spiral form of DnaB provide access to the internal chamber, the combination of contacts by the N-terminal and C-terminal domains of λP-chain Z precludes entry of physiological origin-derived ssDNA into the inner chamber. Deepening the mystery is the finding that the BP complex, nevertheless, still binds ssDNA. On the basis of native mass spectrometry and ATPase rate measurements, we suggest that ssDNA may either bind to the λP

ensemble or on the exterior of DnaB, as previously suggested [102, 103], or both, prior to undergoing necessary conformational changes that enable loading of ssDNA in DnaB's inner chamber.

Asymmetry in the configuration of the five protomers of the λP ensemble provokes questions about mechanisms that mediate helicase opening and ssDNA loading at the origin. λP chain Z leverages its N-terminal and C-terminal lasso domains to span the DnaB breach by contacting the DH element at the breach and the DH-LH junction at the bottom of the DnaB spiral. λP chain Z appears to harbor the elements (e.g., N- and C-terminal lasso/grappling hooks) needed to open the closed planar form of DnaB on its own; if so, what mechanisms are implemented by the C-terminal lassos of the other λP chains? Furthermore, disposition of λP chain Z amino-terminal domain (I/II) across the breached DnaB interface creates an autoinhibited conformation of the BP complex wherein access by physiological ssDNA to the inner chamber is precluded. How is this autoinhibition relieved? We speculate that the autoinhibition will be relieved as the BP complex is recruited to the pre-formed λO•Oriλ complex at the replication origin (Figure 9) and may require intervention by the bacterial heat shock/chaperone proteins: DnaK, DnaJ, and GrpE. Interactions between five N-terminal domains of λP, one ordered and four disordered in the autoinhibited BP complex, and the carboxy-terminal domains of λO could anchor the complex to the λO•Oriλ ensemble, while at the same time stimulating detachment and rotation of domains I/II of λP chain Z to clear the path for ssDNA into the inner chamber, with subsequent detachment of λP chains V:Y.

Additional studies will be required to clarify mechanisms that accompany recruitment of the autoinhibited state of the BP complex to the replication origin.

Data Availability

Coordinates from the X-ray structure of λP – domain III and the cryo-EM structure of the *E. coli* DnaB – λP complex are available from the RCSB Protein Data Bank under accession codes 8V9S and 8V9T, respectively. The underlying primary data, X-ray detector diffraction images, and structure factors, and cryo-EM maps are available from the Protein Data Bank, and the EMBD, under the accession codes 8V9S, 8V9T, and EMD-43086, respectively.

Author Contributions

DB, AS, and DJ conceptualized the study. DB designed and prepared all the λP constructs and purified all the proteins. Crystallization and X-ray crystallography were performed by DB and EI. DB and AS performed the pull-down experiments. AS performed all the ATPase assays. AS and JC acquired and analyzed the cryo-EM data. All native MS analyses were performed by Dom Olinares and Brian Chait. DB, AS, JC, and DJ jointly built and analyzed the structures and drafted the manuscript.

Funding

This work was supported by the National Science Foundation (DJ: MCB 1818255), the National Institutes of Health (DJ: GM08416 and BTC: P41 GM109824 and P41 GM103314), and the Department of Education (JC: PA200A150068). Some of this work was performed at the Simons Electron Microscopy Center and National Resource for Automated Molecular Microscopy

located at the New York Structural Biology Center, supported by grants from the Simons Foundation (SF349247), NYSTAR, and the NIH National Institute of General Medical Sciences (GM103310) with additional support from Agouron Institute (F00316), NIH (OD019994), and NIH (RR029300). This work is based upon research conducted at the Northeastern Collaborative Access Team beamlines, which are funded by the National Institute of General Medical Sciences from the National Institutes of Health (P30 GM124165). The Eiger 16M detector on 24-ID-E is funded by a NIH-ORIP HEI grant (S10OD021527). This research used resources of the Advanced Photon Source; a U.S. Department of Energy (DOE) Office of Science User Facility operated for the DOE Office of Science by Argonne National Laboratory under Contract No. DE-AC02-06CH11357. Funding for the open charge: National Science Foundation MCB #1818255.

Acknowledgements

We thank the members of the Jeruzalmi lab, members of the biophysics group at City College and the CUNY Advanced Science Research Center, and the New York Structural Biology Center for scientific and technical advice. We dedicate our work on the DnaB – λP complex to the memory of Professor Roger McMacken on whose shoulders we stand as we do our work and who inspired us in so many ways.

Conflicts of Interest

The authors have no financial or non-financial conflicts of interest.

References

1. Bleichert F, Botchan MR, Berger JM (2017) Mechanisms for initiating cellular DNA replication. *Science*, 355(6327):eaah6317. https://doi.org/10.1126/science.aah6317

2. Katayama T (2017) DNA Replication, From Old Principles to New Discoveries. *Advances in Experimental Medicine and Biology*, 1042(21):79–98. https://doi.org/10.1007/978-981-10-6955-0_4

3. Yao NY, O'Donnell ME (2016) Evolution of replication machines. *Critical Reviews in Biochemistry and Molecular Biology*, 51(3):135–149. https://doi.org/10.3109/10409238.2015.1125845

4. Yao N, O'Donnell M (2016) Bacterial and Eukaryotic Replisome Machines. *JSM biochemistry and molecular biology*, 3(1)

5. Greci MD, Bell SD (2020) Archaeal DNA Replication. *Annual Review of Microbiology*, 74(1):1–16. https://doi.org/10.1146/annurev-micro-020518-115443

6. Trakselis MA (2016) Structural Mechanisms of Hexameric Helicase Loading, Assembly, and Unwinding. *F1000Research*, 5https://doi.org/10.12688/f1000research.7509.1

7. Blaine HC, Simmons LA, Stallings CL (2023) Diverse Mechanisms of Helicase Loading during DNA Replication Initiation in Bacteria. *Journal of Bacteriology*, 205(4):e00487-22. https://doi.org/10.1128/jb.00487-22

8. Katayama T, Nagata T (1991) Initiation of chromosomal DNA replication which is stimulated without oversupply of DnaA protein in Escherichia coli. *Molecular & general genetics : MGG*, 226(3):491–502.

9. O'Donnell ME, Li H (2018) The ring-shaped hexameric helicases that function at DNA replication forks. *Nature Structural & Molecular Biology*, 25(2):122–130. https://doi.org/10.1038/s41594-018-0024-x

10. Fernandez AJ, Berger JM (2021) Mechanisms of hexameric helicases. *Critical Reviews in Biochemistry and Molecular Biology*, :1–19. https://doi.org/10.1080/10409238.2021.1954597

11. Kaguni JM (2014) DnaA, DnaB, and DnaC. :1–14. https://doi.org/10.1007/978-1-4614-6436-5_142-1

12. Velten M, McGovern S, Marsin S, Ehrlich SD, Noirot P, Polard P (2003) A Two-Protein Strategy for the Functional Loading of a Cellular Replicative DNA

Helicase. *Molecular Cell*, 11(4):1009–1020. https://doi.org/10.1016/s1097-2765(03)00130-8

13. Brézellec P, Vallet-Gely I, Possoz C, Quevillon-Cheruel S, Ferat J-L (2016) DciA is an ancestral replicative helicase operator essential for bacterial replication initiation. *Nature communications*, 7:13271. https://doi.org/10.1038/ncomms13271

14. Brézellec P, Petit M-A, Pasek S, Vallet-Gely I, Possoz C, Ferat J-L (2017) Domestication of lambda phage genes into a putative third type of Replicative Helicase Matchmaker. *Genome Biology and Evolution*, 9(6):evx111. https://doi.org/10.1093/gbe/evx111

15. Marsin S, Adam Y, Cargemel C, Andreani J, Baconnais S, Legrand P, Li de la Sierra-Gallay I, Humbert A, Aumont-Nicaise M, Velours C, Ochsenbein F, Durand D, Le Cam E, Walbott H, Possoz C, Quevillon-Cheruel S, Ferat J-L (2021) Study of the DnaB:DciA interplay reveals insights into the primary mode of loading of the bacterial replicative helicase. *Nucleic Acids Research*, :gkab463-. https://doi.org/10.1093/nar/gkab463

16. Ozaki S, Wang D, Wakasugi Y, Itani N, Katayama T (2022) The Caulobacter crescentus DciA promotes chromosome replication through topological loading of the DnaB replicative helicase at replication forks. *Nucleic Acids Research*, 50(22):gkac1146-. https://doi.org/10.1093/nar/gkac1146

17. Cargemel C, Baconnais S, Aumont-Nicaise M, Noiray M, Maurin L, Andreani J, Walbott H, Cam EL, Ochsenbein F, Marsin S, Quevillon-Cheruel S (2023) Structural Insights of the DciA Helicase Loader in Its Relationship with DNA. *International Journal of Molecular Sciences*, 24(2):1427. https://doi.org/10.3390/ijms24021427

18. Cargemel C, Marsin S, Noiray M, Legrand P, Bounoua H, Sierra-Gallay IL de la, Walbott H, Quevillon-Cheruel S (2022) The LH-DH module of the bacterial replicative helicases is the common binding site for DciA and other helicase loaders. https://doi.org/10.1101/2022.07.08.499335

19. Blaine HC, Burke JT, Ravi J, Stallings CL (2022) DciA Helicase Operators Exhibit Diversity across Bacterial Phyla. *Journal of Bacteriology*, 204(8):e00163-22. https://doi.org/10.1128/jb.00163-22

20. Jones CE, Mueser TC, Dudas KC, Kreuzer KN, Nossal NG (2001) Bacteriophage T4 gene 41 helicase and gene 59 helicase-loading protein: A versatile couple with roles in replication and recombination. *Proceedings of the National Academy of Sciences*, 98(15):8312–8318. https://doi.org/10.1073/pnas.121009398

21. Seco EM, Zinder JC, Manhart CM, Piano AL, McHenry CS, Ayora S (2013) Bacteriophage SPP1 DNA replication strategies promote viral and disable host replication in vitro. *Nucleic Acids Research*, 41(3):1711–1721. https://doi.org/10.1093/nar/gks1290

22. Odegrip R, Schoen S, Haggård-Ljungquist E, Park K, Chattoraj DK (2000) The Interaction of Bacteriophage P2 B Protein with Escherichia coli DnaB Helicase. *Journal of Virology*, 74(9):4057–4063. https://doi.org/10.1128/jvi.74.9.4057-4063.2000

23. Wang G, Klein MG, Tokonzaba E, Zhang Y, Holden LG, Chen XS (2008) The structure of a DnaB-family replicative helicase and its interactions with primase. *Nature Structural & Molecular Biology*, 15(1):94–100. https://doi.org/10.1038/nsmb1356

24. Strycharska MS, Arias-Palomo E, Lyubimov AY, Erzberger JP, O'Shea VL, Bustamante CJ, Berger JM (2013) Nucleotide and Partner-Protein Control of Bacterial Replicative Helicase Structure and Function. *Molecular Cell*, 52(6):844–854. https://doi.org/10.1016/j.molcel.2013.11.016

25. Bailey S, Eliason WK, Steitz TA (2007) Structure of hexameric DnaB helicase and its complex with a domain of DnaG primase. *Science (New York, NY)*, 318(5849):459–463. https://doi.org/10.1126/science.1147353

26. Itsathitphaisarn O, Wing RA, Eliason WK, Wang J, Steitz TA (2012) The Hexameric Helicase DnaB Adopts a Nonplanar Conformation during Translocation. *Cell*, 151(2):267–277. https://doi.org/10.1016/j.cell.2012.09.014

27. Kaguni JM (2018) The Macromolecular Machines that Duplicate the Escherichia coli Chromosome as Targets for Drug Discovery. *Antibiotics*, 7(1):23. https://doi.org/10.3390/antibiotics7010023

28. Chodavarapu S, Kaguni JM (2016) Replication Initiation in Bacteria. 39:1–30. https://doi.org/10.1016/bs.enz.2016.03.001

29. O'Donnell M, Langston L, Stillman B (2013) Principles and concepts of DNA replication in bacteria, archaea, and eukarya. *Cold Spring Harbor perspectives in biology*, 5(7):a010108–a010108. https://doi.org/10.1101/cshperspect.a010108

30. Bell SP, Kaguni JM (2013) Helicase loading at chromosomal origins of replication. *Cold Spring Harbor perspectives in biology*, 5(6):a010124. https://doi.org/10.1101/cshperspect.a010124

31. Kaguni JM (2013) DNA Replication: Initiation in Bacteria. :121–125. https://doi.org/10.1016/b978-0-12-378630-2.00313-3

32. Wolański M, Donczew R, Zawilak-Pawlik A, Zakrzewska-Czerwińska J (2014) oriC-encoded instructions for the initiation of bacterial chromosome replication. *Frontiers in microbiology*, 5:735. https://doi.org/10.3389/fmicb.2014.00735

33. Oakley AJ (2019) A structural view of bacterial DNA replication. *Protein Science*, 28(6):990–1004. https://doi.org/10.1002/pro.3615

34. Zylicz M, Ang D, Liberek K, Georgopoulos C (1989) Initiation of lambda DNA replication with purified host- and bacteriophage-encoded proteins: the role of the dnaK, dnaJ and grpE heat shock proteins. *The EMBO Journal*, 8(5):1601–1608. https://doi.org/10.1002/j.1460-2075.1989.tb03544.x

35. Liberek K, Georgopoulos C, Zylicz M (1988) Role of the Escherichia coli DnaK and DnaJ heat shock proteins in the initiation of bacteriophage lambda DNA replication. *Proceedings of the National Academy of Sciences*, 85(18):6632–6636. https://doi.org/10.1073/pnas.85.18.6632

36. Hoffmann HJ, Lyman SK, Lu C, Petit MA, Echols H (1992) Activity of the Hsp70 chaperone complex--DnaK, DnaJ, and GrpE--in initiating phage lambda DNA replication by sequestering and releasing lambda P protein. *Proceedings of the National Academy of Sciences*, 89(24):12108–12111. https://doi.org/10.1073/pnas.89.24.12108

37. Osipiuk J, Georgopoulos C, Zylicz M (1993) Initiation of lambda DNA replication. The Escherichia coli small heat shock proteins, DnaJ and GrpE, increase DnaK's affinity for the lambda P protein. *Journal of Biological Chemistry*, 268(7):4821–4827. https://doi.org/10.1016/s0021-9258(18)53470-0

38. O'Shea VL, Berger JM (2014) Loading strategies of ring-shaped nucleic acid translocases and helicases. *Current Opinion in Structural Biology*, 25:16–24. https://doi.org/10.1016/j.sbi.2013.11.006

39. Davey MJ, O'Donnell M (2003) Replicative helicase loaders: ring breakers and ring makers. *Current Biology*, 13(15):R594–R596. https://doi.org/10.1016/s0960-9822(03)00523-2

40. Chase J, Catalano A, Noble AJ, Eng ET, Olinares PD, Molloy K, Pakotiprapha D, Samuels M, Chait B, Georges AD, Jeruzalmi D (2018) Mechanisms of opening and closing of the bacterial replicative helicase. *eLife*, 7:1822. https://doi.org/10.7554/elife.41140

41. Arias-Palomo E, Puri N, Murray VLO, Yan Q, Berger JM (2019) Physical Basis for the Loading of a Bacterial Replicative Helicase onto DNA. *Molecular Cell*, 74(1):173-184.e4. https://doi.org/10.1016/j.molcel.2019.01.023

42. Arias-Palomo E, O'Shea VL, Hood IV, Berger JM (2013) The Bacterial DnaC Helicase Loader Is a DnaB Ring Breaker. *Cell*, 153(2):438–448. https://doi.org/10.1016/j.cell.2013.03.006

43. Costa A, Diffley JFX (2022) The Initiation of Eukaryotic DNA Replication. *Annual Review of Biochemistry*, 91(1):107–131. https://doi.org/10.1146/annurev-biochem-072321-110228

44. Attali I, Botchan MR, Berger JM (2021) Structural Mechanisms for Replicating DNA in Eukaryotes. *Annual Review of Biochemistry*, 90(1):1–30. https://doi.org/10.1146/annurev-biochem-090120-125407

45. Chase J, Berger J, Jeruzalmi D (2022) Convergent evolution in two bacterial replicative helicase loaders. *Trends in Biochemical Sciences*, 47(7):620–630. https://doi.org/10.1016/j.tibs.2022.02.005

46. Jumper J, Evans R, Pritzel A, Green T, Figurnov M, Ronneberger O, Tunyasuvunakool K, Bates R, Žídek A, Potapenko A, Bridgland A, Meyer C, Kohl SAA, Ballard AJ, Cowie A, Romera-Paredes B, Nikolov S, Jain R, Adler J, Back T, Petersen S, Reiman D, Clancy E, Zielinski M, Steinegger M, Pacholska M, Berghammer T, Bodenstein S, Silver D, Vinyals O, Senior AW, Kavukcuoglu K, Kohli P, Hassabis D (2021) Highly accurate protein structure prediction with AlphaFold. *Nature*, 596(7873):583–589. https://doi.org/10.1038/s41586-021-03819-2

47. Varadi M, Anyango S, Deshpande M, Nair S, Natassia C, Yordanova G, Yuan D, Stroe O, Wood G, Laydon A, Žídek A, Green T, Tunyasuvunakool K, Petersen S, Jumper J, Clancy E, Green R, Vora A, Lutfi M, Figurnov M, Cowie A, Hobbs N, Kohli P, Kleywegt G, Birney E, Hassabis D, Velankar S (2021) AlphaFold Protein Structure Database: massively expanding the structural coverage of protein-sequence space with high-accuracy models. *Nucleic Acids Research*, 50(D1):D439–D444. https://doi.org/10.1093/nar/gkab1061

48. Orlova N, Gerding M, Ivashkiv O, Olinares PDB, Chait BT, Waldor MK, Jeruzalmi D (2017) The replication initiator of the cholera pathogen's second chromosome shows structural similarity to plasmid initiators. *Nucleic Acids Research*, 45(7):3724–3737. https://doi.org/10.1093/nar/gkw1288

49. Kantardjieff KA, Rupp B (2003) Matthews coefficient probabilities: Improved estimates for unit cell contents of proteins, DNA, and protein-nucleic acid complex crystals. *Protein science : a publication of the Protein Society*, 12(9):1865–1871. https://doi.org/10.1110/ps.0350503

50. Otwinowski Z, Minor W (1997) Processing of X-ray diffraction data collected in oscillation mode. *Macromolecular Crystallography, Pt A*, 276:307–326.

51. Liebschner D, Afonine PV, Baker ML, Bunkóczi G, Chen VB, Croll TI, Hintze B, Hung LW, Jain S, McCoy AJ, Moriarty NW, Oeffner RD, Poon BK, Prisant MG, Read RJ, Richardson JS, Richardson DC, Sammito MD, Sobolev OV, Stockwell DH, Terwilliger TC, Urzhumtsev AG, Videau LL, Williams CJ, Adams PD (2019) Macromolecular structure determination using X-rays, neutrons and electrons: recent developments in Phenix. *Acta Crystallographica Section D: Structural Biology*, 75(10):861–877. https://doi.org/10.1107/s2059798319011471

52. Emsley P, Lohkamp B, Scott WG, Cowtan K (2010) Features and development of Coot. *Acta crystallographica Section D, Biological crystallography*, 66(Pt 4):486–501. https://doi.org/10.1107/s0907444910007493

53. Learn BA, Um SJ, Huang L, McMacken R (1997) Cryptic single-stranded-DNA binding activities of the phage lambda P and Escherichia coli DnaC replication initiation proteins facilitate the transfer of E. coli DnaB helicase onto DNA. *Proceedings of the National Academy of Sciences of the United States of America*, 94(4):1154–1159. https://doi.org/10.1073/pnas.94.4.1154

54. Olinares PDB, Chait BT (2019) The Eukaryotic RNA Exosome, Methods and Protocols. *Methods in Molecular Biology*, 2062:357–382. https://doi.org/10.1007/978-1-4939-9822-7_17

55. Reid DJ, Diesing JM, Miller MA, Perry SM, Wales JA, Montfort WR, Marty MT (2019) MetaUniDec: High-Throughput Deconvolution of Native Mass Spectra. *Journal of The American Society for Mass Spectrometry*, 30(1):118–127. https://doi.org/10.1007/s13361-018-1951-9

56. Marty MT, Baldwin AJ, Marklund EG, Hochberg GKA, Benesch JLP, Robinson CV (2015) Bayesian Deconvolution of Mass and Ion Mobility Spectra: From Binary Interactions to Polydisperse Ensembles. *Analytical Chemistry*, 87(8):4370–4376. https://doi.org/10.1021/acs.analchem.5b00140

57. Lindsley JE (2000) DNA Topoisomerase Protocols. *Methods in molecular biology (Clifton, N.J.)*, 95:57–64. https://doi.org/10.1385/1-59259-057-8:57

58. Kiianitsa K, Solinger JA, Heyer W-D (2003) NADH-coupled microplate photometric assay for kinetic studies of ATP-hydrolyzing enzymes with low and high specific activities. *Analytical Biochemistry*, 321(2):266–271. https://doi.org/10.1016/s0003-2697(03)00461-5

59. Suloway C, Pulokas J, Fellmann D, Cheng A, Guerra F, Quispe J, Stagg S, Potter CS, Carragher B (2005) Automated molecular microscopy: the new Leginon system. *Journal of structural biology*, 151(1):41–60. https://doi.org/10.1016/j.jsb.2005.03.010

60. Noble AJ, Dandey VP, Wei H, Braschi J, Chase J, Acharya P, Tan YZ, Zhang Z, Kim LY, Scapin G, Rapp M, Eng ET, Rice WJ, Cheng A, Negro CJ, Shapiro L, Kwong PD, Jeruzalmi D, Georges AD, Potter CS, Carragher B (2018) Routine single particle cryoEM sample and grid characterization by tomography. *eLife*, 7https://doi.org/10.7554/elife.34257

61. Tegunov D, Cramer P (2019) Real-time cryo-electron microscopy data preprocessing with Warp. *Nature Methods*, 16(11):1146–1152. https://doi.org/10.1038/s41592-019-0580-y

62. Punjani A, Zhang H, Fleet DJ (2020) Non-uniform refinement: adaptive regularization improves single-particle cryo-EM reconstruction. *Nature Methods*, 17(12):1214–1221. https://doi.org/10.1038/s41592-020-00990-8

63. Punjani A, Fleet DJ (2021) 3D variability analysis: Resolving continuous flexibility and discrete heterogeneity from single particle cryo-EM. *Journal of Structural Biology*, 213(2):107702. https://doi.org/10.1016/j.jsb.2021.107702

64. Punjani A, Rubinstein JL, Fleet DJ, Brubaker MA (2017) cryoSPARC: algorithms for rapid unsupervised cryo-EM structure determination. *Nature Methods*, 14(3):290–296. https://doi.org/10.1038/nmeth.4169

65. Sanchez-Garcia R, Gomez-Blanco J, Cuervo A, Carazo JM, Sorzano COS, Vargas J (2021) DeepEMhancer: a deep learning solution for cryo-EM volume post-processing. *Communications Biology*, 4(1):874. https://doi.org/10.1038/s42003-021-02399-1

66. Vagin A, Teplyakov A (2010) Molecular replacement with MOLREP. *Acta crystallographica Section D, Biological crystallography*, 66(Pt 1):22–25. https://doi.org/10.1107/s0907444909042589

67. Vagin AA, Isupov MN (2001) Spherically averaged phased translation function and its application to the search for molecules and fragments in electron-density maps. *Acta crystallographica Section D, Biological crystallography*, 57(Pt 10):1451–1456.

68. Vagin A, Teplyakov A (2000) An approach to multi-copy search in molecular replacement. *Acta crystallographica Section D, Biological crystallography*, 56(Pt 12):1622–1624.

69. Winn MD, Ballard CC, Cowtan KD, Dodson EJ, Emsley P, Evans PR, Keegan RM, Krissinel EB, Leslie AGW, McCoy A, McNicholas SJ, Murshudov GN, Pannu NS, Potterton EA, Powell HR, Read RJ, Vagin A, Wilson KS (2011) Overview of the CCP4 suite and current developments. *Acta crystallographica Section D, Biological crystallography*, 67(Pt 4):235–242. https://doi.org/10.1107/s0907444910045749

70. Pettersen EF, Goddard TD, Huang CC, Couch GS, Greenblatt DM, Meng EC, Ferrin TE (2004) UCSF Chimera--a visualization system for exploratory research and analysis. *Journal of computational chemistry*, 25(13):1605–1612. https://doi.org/10.1002/jcc.20084

71. Fass D, Bogden CE, Berger JM (1999) Crystal structure of the N-terminal domain of the DnaB hexameric helicase. *Structure (London, England : 1993)*, 7(6):691–698. http://linkinghub.elsevier.com/retrieve/pii/S0969212699800902

72. Brown A, Long F, Nicholls RA, Toots J, Emsley P, Murshudov G (2015) Tools for macromolecular model building and refinement into electron cryo-microscopy reconstructions. *Acta crystallographica Section D, Biological crystallography*, 71(1):136–153. https://doi.org/10.1107/s1399004714021683

73. Emsley P, Cowtan K (2004) Coot: model-building tools for molecular graphics. *Acta crystallographica Section D, Biological crystallography*, 60(Pt 12 Pt 1):2126–2132. https://doi.org/10.1107/s0907444904019158

74. Kleywegt G, Zou J, Kjeldgaard M, Jones T (2001) International Tables for Crystallography, Vol. F, edited by MG Rossmann & E. Arnold, ch. 17.1, pp. 353ą356, 366ą367.

75. Sierk M, Kleywegt G (2004) Deja Vu All Over Again: Finding and Analyzing Protein Structure Similarities. *Structure (London, England : 1993)*, 12(12):2103–2111. http://www.sciencedirect.com/science/article/B6VSR-4DYV1YN-5/2/e51c106caee53525bdc042ff03413ba7

76. Kleywegt GJ (2007) Quality control and validation. *Methods in molecular biology (Clifton, NJ)*, 364:255–272. https://doi.org/10.1385/1-59745-266-1:255

77. Kleywegt G, Jones T (1997) Model building and refinement practice. *Macromolecular Crystallography, Pt A*, 277:208–230.

78. Williams CJ, Headd JJ, Moriarty NW, Prisant MG, Videau LL, Deis LN, Verma V, Keedy DA, Hintze BJ, Chen VB, Jain S, Lewis SM, Arendall WB, Snoeyink J, Adams PD, Lovell SC, Richardson JS, Richardson DC (2018) MolProbity: More and better reference data for improved all-atom structure validation. *Protein Science*, 27(1):293–315. https://doi.org/10.1002/pro.3330

79. Echols N, Moriarty NW, Klei HE, Afonine PV, Bunkóczi G, Headd JJ, Mccoy AJ, Oeffner RD, Read RJ, Terwilliger TC, Adams PD (2014) Automating crystallographic structure solution and refinement of protein-ligand complexes. *Acta crystallographica Section D, Biological crystallography*, 70(Pt 1):144–154. https://doi.org/10.1107/s139900471302748x

80. Zwart PH, Afonine PV, Grosse-Kunstleve RW, Hung L-W, Ioerger TR, Mccoy AJ, McKee E, Moriarty NW, Read RJ, Sacchettini JC, Sauter NK, Storoni LC, Terwilliger TC, Adams PD (2008) Automated structure solution with the PHENIX suite. *Methods in molecular biology (Clifton, NJ)*, 426:419–435. https://doi.org/10.1007/978-1-60327-058-8_28

81. Afonine PV, Poon BK, Read RJ, Sobolev OV, Terwilliger TC, Urzhumtsev A, Adams PD (2018) Real-space refinement in PHENIX for cryo-EM and crystallography. *Acta Crystallographica Section D*, 74(6):531–544. https://doi.org/10.1107/s2059798318006551

82. Terwilliger TC, Read RJ, Adams PD, Brunger AT, Afonine PV, Hung L-W (2013) Model morphing and sequence assignment after molecular replacement. *Acta Crystallographica Section D: Biological Crystallography*, 69(11):2244–2250. https://doi.org/10.1107/s0907444913017770

83. Afonine PV, Grosse-Kunstleve RW, Echols N, Headd JJ, Moriarty NW, Mustyakimov M, Terwilliger TC, Urzhumtsev A, Zwart PH, Adams PD (2012) Towards automated crystallographic structure refinement with phenix.refine. *Acta crystallographica Section D, Biological crystallography*, 68(Pt 4):352–367. https://doi.org/10.1107/s0907444912001308

84. Adams PD, Afonine PV, Bunkóczi G, Chen VB, Davis IW, Echols N, Headd JJ, Hung L-W, Kapral GJ, Grosse-Kunstleve RW, Mccoy AJ, Moriarty NW, Oeffner R, Read RJ, Richardson DC, Richardson JS, Terwilliger TC, Zwart PH (2010) PHENIX: a comprehensive Python-based system for macromolecular structure solution. *Acta crystallographica Section D, Biological crystallography*, 66(Pt 2):213–221. https://doi.org/10.1107/s0907444909052925

85. LLC S , (2017) The PyMOL Molecular Graphics System, Version 2.1.

86. Morin A, Eisenbraun B, Key J, Sanschagrin PC, Timony MA, Ottaviano M, Sliz P (2013) Collaboration gets the most out of software. *eLife*, 2:e01456. https://doi.org/10.7554/elife.01456

87. Cruz MJ de la, Eng ET (2023) Scaling up cryo-EM for biology and chemistry: The journey from niche technology to mainstream method. *Structure*, https://doi.org/10.1016/j.str.2023.09.009

88. Saibil HR (2022) Cryo-EM in molecular and cellular biology. *Molecular Cell*, 82(2):274–284. https://doi.org/10.1016/j.molcel.2021.12.016

89. Guaita M, Watters SC, Loerch S (2022) Recent advances and current trends in cryo-electron microscopy. *Current Opinion in Structural Biology*, 77:102484. https://doi.org/10.1016/j.sbi.2022.102484

90. Chari A, Stark H (2023) Prospects and Limitations of High-Resolution Single-Particle Cryo-Electron Microscopy. *Annual Review of Biophysics*, 52(1):391–411. https://doi.org/10.1146/annurev-biophys-111622-091300

91. Hayes S, Erker C, Horbay M, Marciniuk K, Wang W, Hayes C (2013) Phage Lambda P Protein: Trans-Activation, Inhibition Phenotypes and their Suppression. *Viruses*, 5(2):619–653. https://doi.org/10.3390/v5020619

92. Mallory JB, Alfano C, McMacken R (1990) Host virus interactions in the initiation of bacteriophage lambda DNA replication. Recruitment of Escherichia coli DnaB helicase by lambda P replication protein. *Journal of Biological Chemistry*, 265(22):13297–13307. https://doi.org/10.1016/s0021-9258(19)38298-5

93. Leipe DD, Aravind L, Grishin NV, Koonin EV (2000) The bacterial replicative helicase DnaB evolved from a RecA duplication. *Genome research*, 10(1):5–16. https://doi.org/10.1101/gr.10.1.5

94. Oakley AJ, Xu ZQ (2022) E. coli DnaB bound to ssDNA and AMPPNP. https://doi.org/10.2210/pdb7t20/pdb

95. Oakley AJ, Xu ZQ (2023) E. coli DnaB bound to ssDNA and ADP-AlF4. https://doi.org/10.2210/pdb7t21/pdb

96. Oakley AJ, Xu ZQ (2023) E. coli DnaB bound to three DnaG C-terminal domains, ssDNA, ADP and AlF4. https://doi.org/10.2210/pdb7t22/pdb

97. Oakley AJ, Xu ZQ (2023) E. coli DnaB bound to two DnaG C-terminal domains, ssDNA, ADP and AlF4. https://doi.org/10.2210/pdb7t23/pdb

98. Marsin S, Adam Y, Cargemel C, Andreani J, Baconnais S, Legrand P, Li de la Sierra-Gallay I, Humbert A, Aumont-Nicaise M, Velours C, Ochsenbein F, Durand D, Le Cam E, Walbott H, Possoz C, Quevillon-Cheruel S, Ferat J-L (2021) Study of the DnaB:DciA interplay reveals insights into the primary mode of loading of the bacterial replicative helicase. *Nucleic Acids Research*, 49(11):gkab463-. https://doi.org/10.1093/nar/gkab463

99. Jezewska MJ, Kim US, Bujalowski W (1996) Interactions of Escherichia coli primary replicative helicase DnaB protein with nucleotide cofactors. *Biophysical Journal*, 71(4):2075–2086. https://doi.org/10.1016/s0006-3495(96)79406-7

100. Wiegand T, Cadalbert R, Lacabanne D, Timmins J, Terradot L, Böckmann A, Meier BH (2019) The conformational changes coupling ATP hydrolysis and translocation in a bacterial DnaB helicase. *Nature Communications*, 10(1):31. https://doi.org/10.1038/s41467-018-07968-3

101. Crampton DJ, Guo S, Johnson DE, Richardson CC (2004) The arginine finger of bacteriophage T7 gene 4 helicase: Role in energy coupling. *Proceedings of the National Academy of Sciences*, 101(13):4373–4378. https://doi.org/10.1073/pnas.0400968101

102. Carney SM, Gomathinayagam S, Leuba SH, Trakselis MA (2017) Bacterial DnaB helicase interacts with the excluded strand to regulate unwinding. *Journal of Biological Chemistry*, 292(46):19001–19012. https://doi.org/10.1074/jbc.m117.814178

103. Behrmann MS, Perera HM, Hoang JM, Venkat TA, Visser BJ, Bates D, Trakselis MA (2021) Targeted chromosomal Escherichia coli:dnaB exterior surface residues regulate DNA helicase behavior to maintain genomic stability and organismal fitness. *PLoS Genetics*, 17(11):e1009886. https://doi.org/10.1371/journal.pgen.1009886

104. Lee JY, Yang W (2006) UvrD helicase unwinds DNA one base pair at a time by a two-part power stroke. *Cell*, 127(7):1349–1360. https://doi.org/10.1016/j.cell.2006.10.049

105. Pakotiprapha D, Samuels M, Shen K, Hu JH, Jeruzalmi D (2012) Structure and mechanism of the UvrA-UvrB DNA damage sensor. *Nature structural & molecular biology*, 19(3):291–8. https://doi.org/10.1038/nsmb.2240

106. Hamann F, Schmitt A, Favretto F, Hofele R, Neumann P, Xiang S, Urlaub H, Zweckstetter M, Ficner R (2020) Structural analysis of the intrinsically disordered splicing factor Spp2 and its binding to the DEAH-box ATPase Prp2. *Proceedings of the National Academy of Sciences*, 117(6):2948–2956. https://doi.org/10.1073/pnas.1907960117

107. Thomsen ND, Berger JM (2009) Running in Reverse: The Structural Basis for Translocation Polarity in Hexameric Helicases. *Cell*, 139(3):523–534. https://doi.org/10.1016/j.cell.2009.08.043

108. Xing X, Bell CE (2004) Crystal Structures of Escherichia coli RecA in Complex with MgADP and MnAMP−PNP † , ‡. *Biochemistry*, 43(51):16142–16152. https://doi.org/10.1021/bi048165y

109. Abrahams JP, Leslie AG, Lutter R, Walker JE (1994) Structure at 2.8 A resolution of F1-ATPase from bovine heart mitochondria. *Nature*, 370(6491):621–628. https://doi.org/10.1038/370621a0

Figures/Figure legends

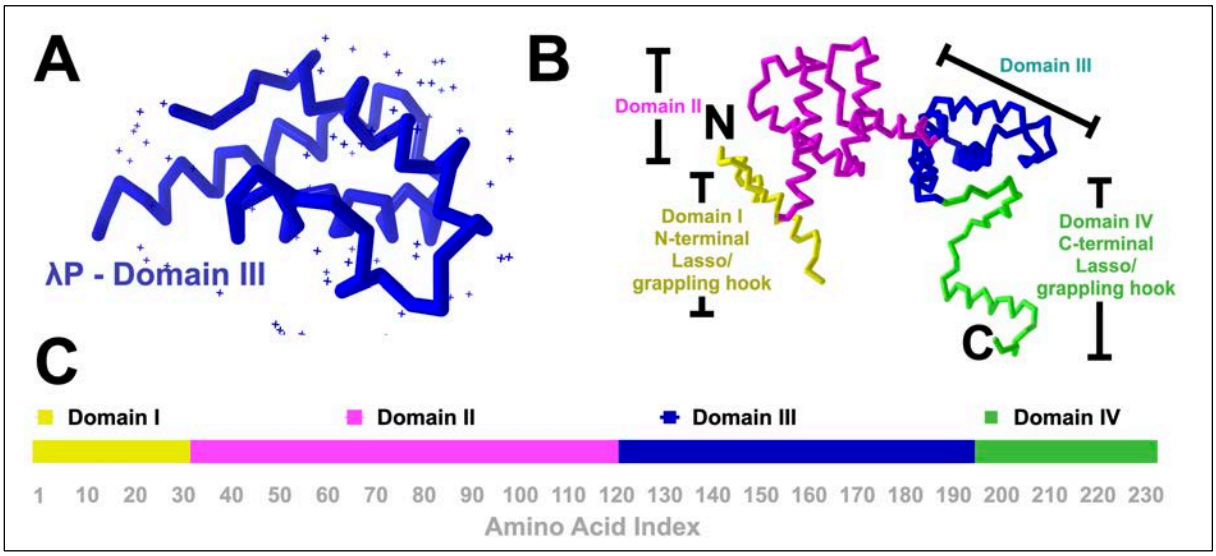

Figure 1. The Complete Structure of the λP Helicase Loader. A) PyMol ribbon representation of the 1.86 Å crystal structure of λP domain III. Water molecules in the structure are depicted as plus (+) signs. B) The Alphafold calculated model of the complete λP helicase loader. C) Linear domain map of λP. The model in B is colored by domain as shown in C.

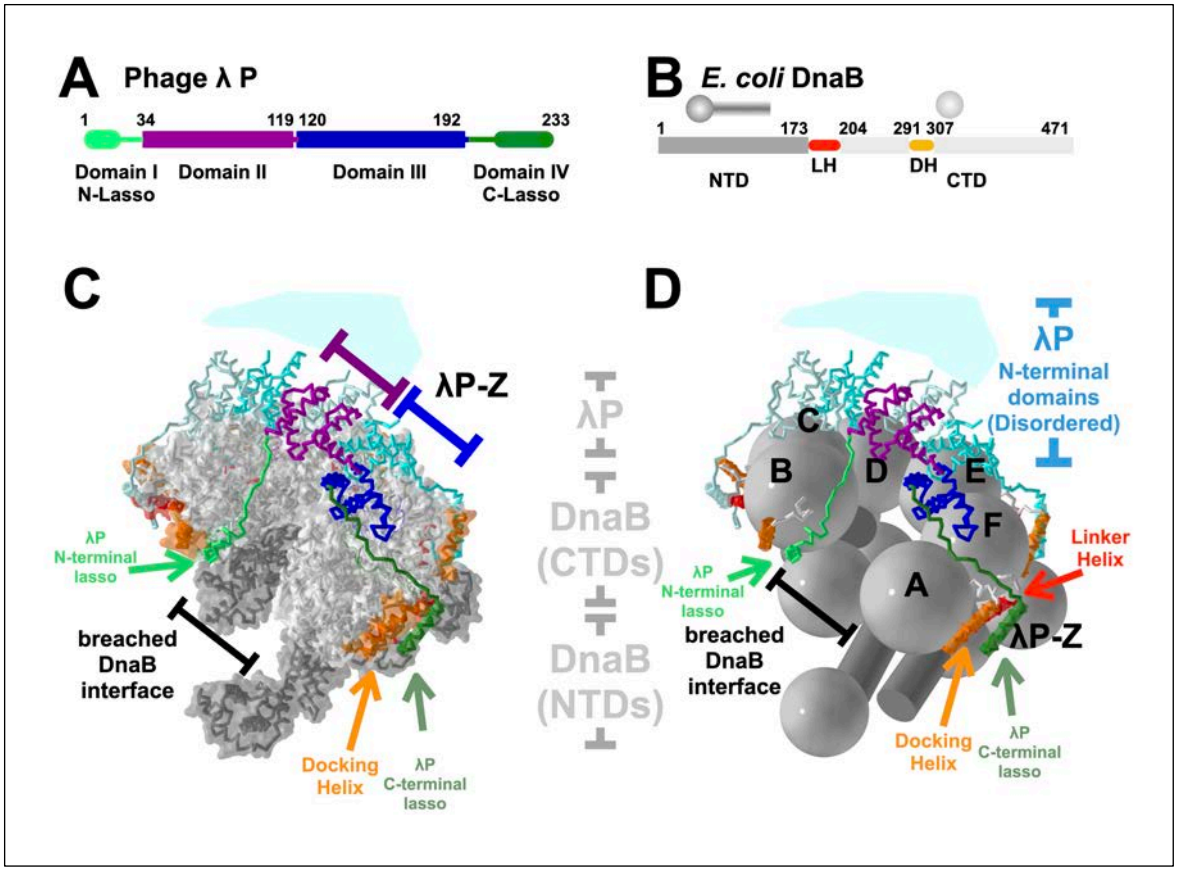

Figure 2. The Structure of the *E. coli* DnaB – λP loader. A) Linear domain architecture of λP. B) Linear domain architecture of *E. coli* DnaB. The amino (NTD) and carboxy-terminal (CTD) layers of DnaB are shown using a design language that depicts the CTDs as large spheres and the NTDs as small spheres/cylinder. C) The DnaB – λP complex, with its five loader molecules depicted in the ribbon representation and colored in shades of blue. The complete structure of λP chain Z is modeled and depicted colored by domain as in Figure 2A. DnaB is colored as in panel 2B, with the DH and LH elements colored and labeled in orange and yellow, respectively. The right-handed open spiral of DnaB is depicted in the ribbon representation superimposed by a transparent surface. The light blue shape above the complex marks the space expected to be occupied

by the disordered amino-terminal domains of λP. D) Same as panel C, except that DnaB is depicted using the design language described above. The CTD spheres of each subunit carry labels corresponding to the underlying chain. Only λP chain Z is labeled.

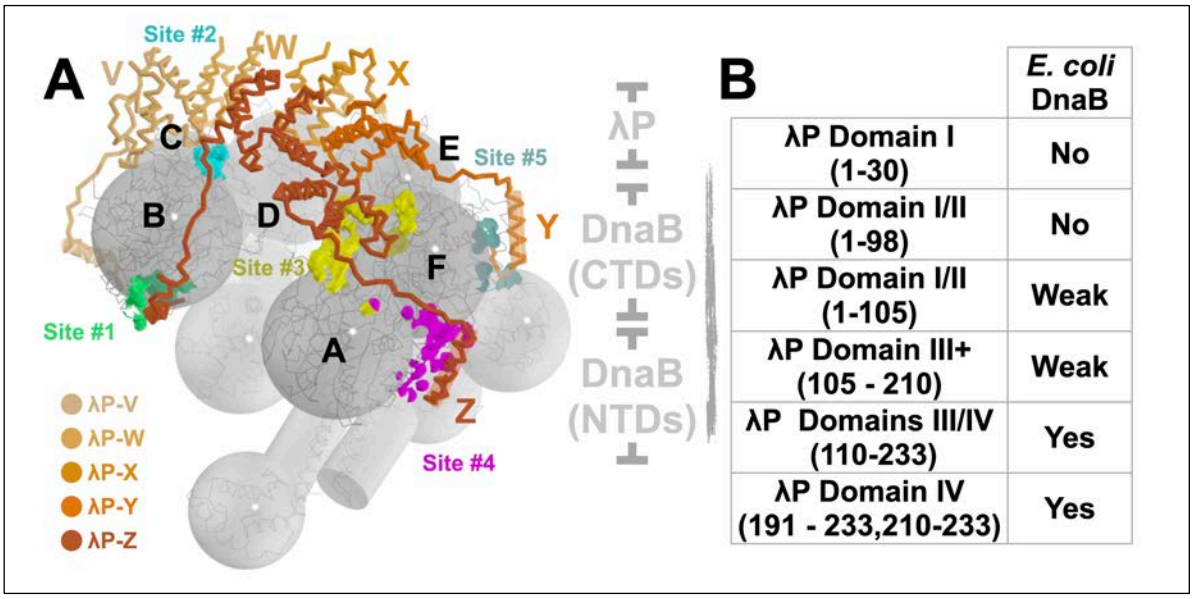

	E. coli DnaB
λP Domain I (1-30)	No
λP Domain I/II (1-98)	No
λP Domain I/II (1-105)	Weak
λP Domain III+ (105 - 210)	Weak
λP Domains III/IV (110-233)	Yes
λP Domain IV (191 - 233,210-233)	Yes

Figure 3. The Interface between the λP loader Helicase Loader and *E. coli* DnaB Encompasses Five Widely Dispersed Sites. A) The five sites of interaction (#1 - 5, colored accordingly) between subunits of the loader and the helicase. Owing to the asymmetry of the BP complex, not every loader protomer employs each site. The λP ensemble is depicted in ribbon format, colored on shades of orange as indicated in the legend. The DnaB hexamer, with subunits labeled A to F, is depicted in a ribbon and abstract shape design language. The CTD spheres of each subunit carry labels corresponding to the underlying chain. B) Summary of binding experiments (detailed in Supplementary Figure 2S) between various constructions of λP and full-length *E. coli* DnaB. λP Domain III+ indicates that 105-210 includes a part of domain IV.

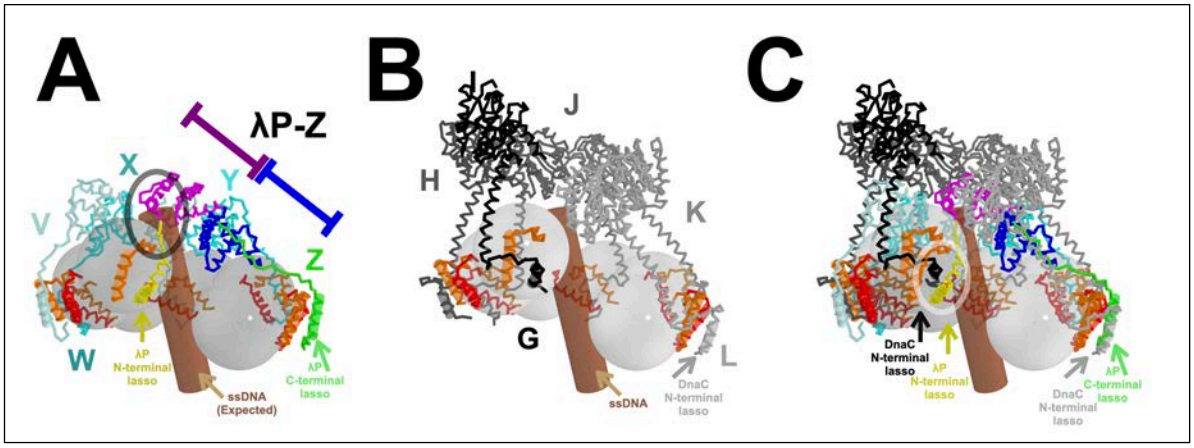

Figure 4. Asymmetry and Convergent Evolution in the λP ensemble. A) In contrast to the other chains, which bind to two DnaB subunits, λP chain Z binds to three subunits, two (chain A and B) of which are located on either side of the breached DnaB interface. This disposition of the amino-terminal domain (domains I/II) of λP chain Z effectively precludes entry of a physiological origin ssDNA into the central chamber of DnaB. λP chain Z is colored as in Figure 1, the remaining λP chains are colored in shades of cyan. The brown cylinder suggested the expected position of ssDNA based on the DnaB-DnaC-ssDNA complex (PDB: 6QEM, [41]). The DnaB CTD are depicted as transparent grey spheres with labels corresponding to the underlying chain; for clarity, the NTD domains are not shown. The DnaB DH and LH helices are colored in red and orange, respectively. λP chain Z blocks entry of ssDNA into the central DnaB chamber (highlighted by the molecular clash which is circled in gray). B) The DnaB-DnaC-ssDNA complex (PDB: 6QEM) posed as superimposed on chain A of the BP complex and depicted in the same style as the BP complex in panel A. Individual DnaC protomers are colored in shades of gray. C) The BP and BC loader complexes in panels A and B are shown simultaneously. Each of the C-terminal lassos from λP superimposes

on a DnaC lasso. However, the single visible N-terminal lasso overlaps with the position of the DnaC lasso at the top of the spiral. The gray circle shows that the N-terminal lasso of λP chain Z overlaps with the DnaC lasso chain G. Thus, one λP subunit makes contacts to DnaB that are made by two DnaC loader subunits.

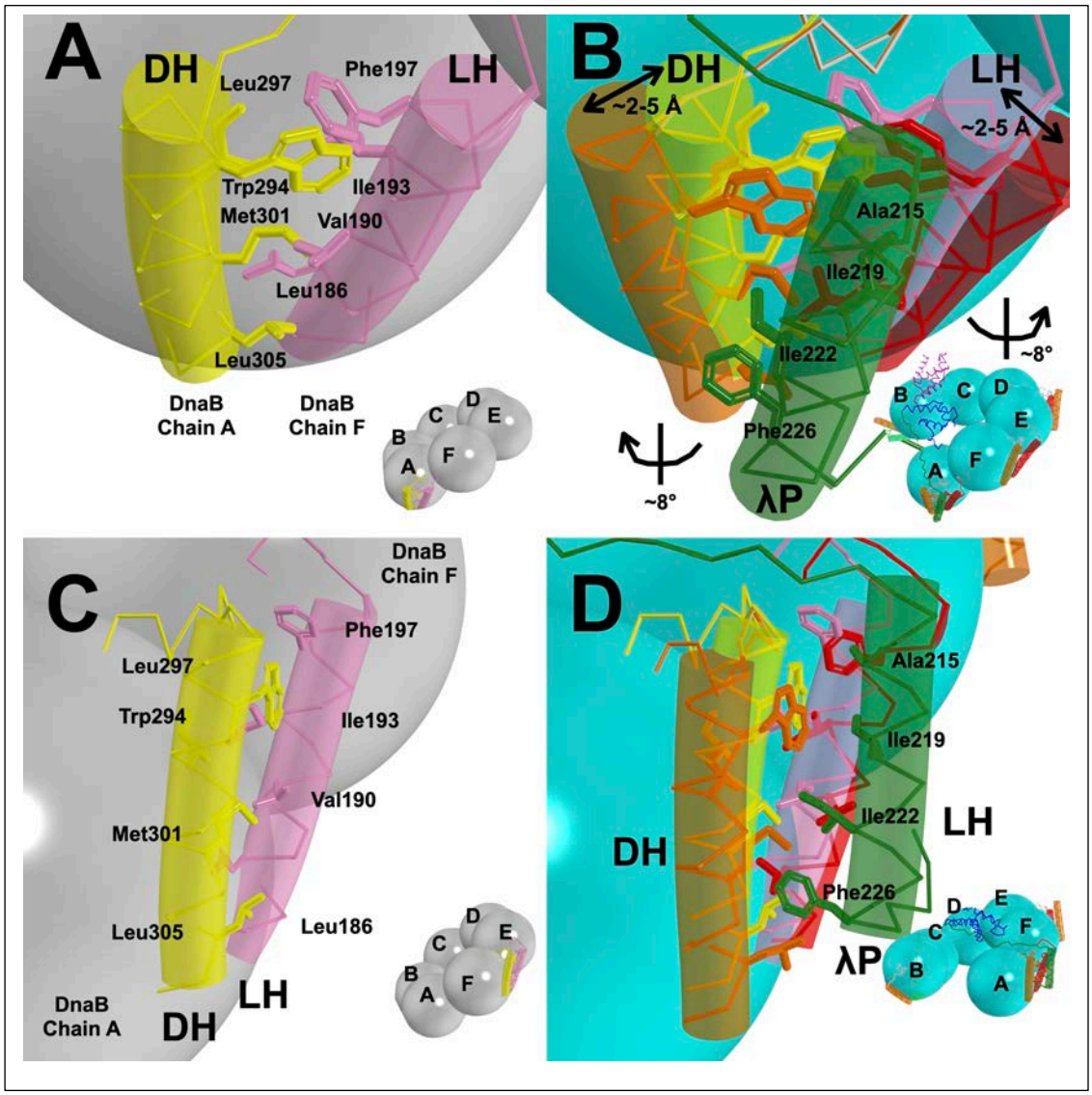

Figure 5. The Carboxy-Terminal Domain of the λP Ensemble Shears the LH-DH Interface of Each DnaB Monomer. A) Knobs and holes packing interactions between the docking helix (DH) and linker helix (LH) in the closed planar form of *E. coli*. DnaB. The above model was constructed by superimposing the DH and LH helices on the closed planar DnaB model from *Aquifex aeolicus* (PDB: 4NMN, [24]). Residues 291:306 (DH) and 182:199 (LH) are depicted in the PyMol ribbon and transparent cylindrical cartoon representation. B) The λP loader disrupts the

DH – LH interaction during transition from the closed planar to the open spiral form of E. coli DnaB. The DH and LH helices rotate by 8° and 2-5 Å away from the dimer interface during the transition. The disrupted DH – LH interaction is replaced by hydrophobic interactions with the C-terminal lasso helix of λP. The depictions in panels C and D are identical to panels A and B, respectively, save for an ~90°rotation about the vertical axis. Each panel includes an inset which depicts the appropriate complete DnaB hexamer with each CTD drawn as a sphere; for clarity, the NTD domains are not shown. The letters on each inset represents various protein chains of the DnaB hexamer.

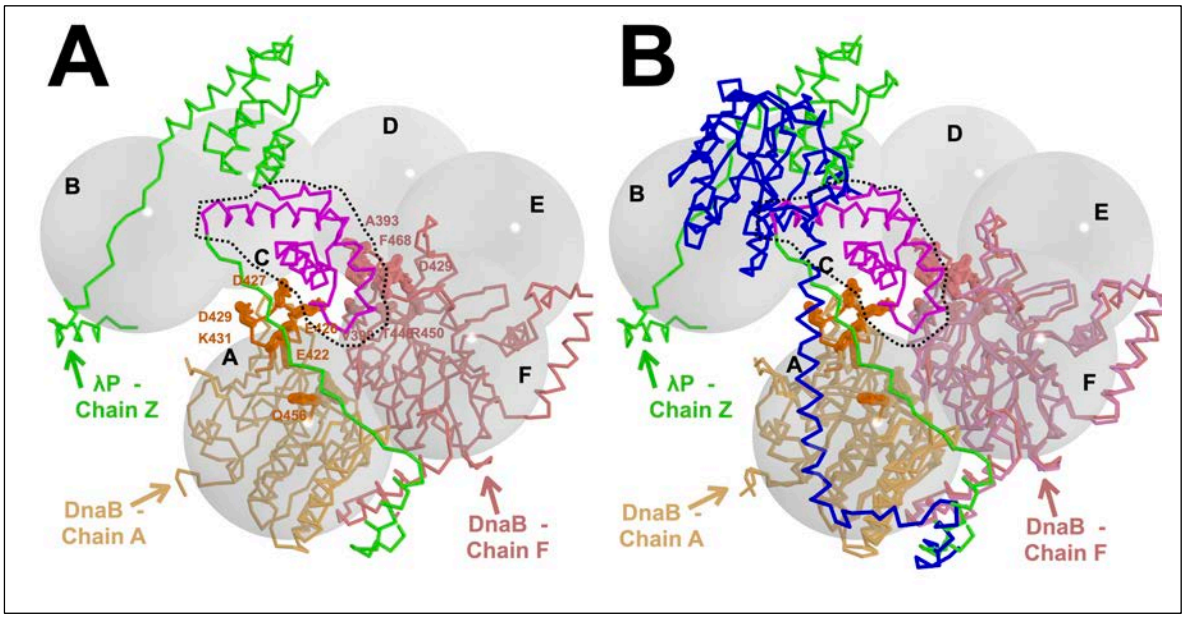

Figure 6. Stabilization of the DnaB Spiral by Domain III of λP. The open spiral of DnaB is stabilized via contacts to domain III of the λP loader. Schematic view of the BP complex wherein the CTDs in the open spiral are represented by transparent and labeled grey spheres. Chain Z of the λP ensemble (green) is shown in the PyMol ribbon representation, as are the CTDs from chain A (light orange) and chain F (salmon). Residues in the DnaB CTD from Chain A (light orange) and chain F (salmon) that contact domain III of λP (outlined) are shown using the stick representation. For clarity the corresponding interfacial residues on chain λP Z are not shown. Panel A shows the BP complex, while panel B shows the BP complex with one DnaC chain from the DnaB-DnaC (in this pose, chain F of PDB: 6QEL, [41], superimposed on chain A of the BP complex and residues 206:468, but not residues 181:196 (LH) or residues 290:306 (DH) shown (blue).

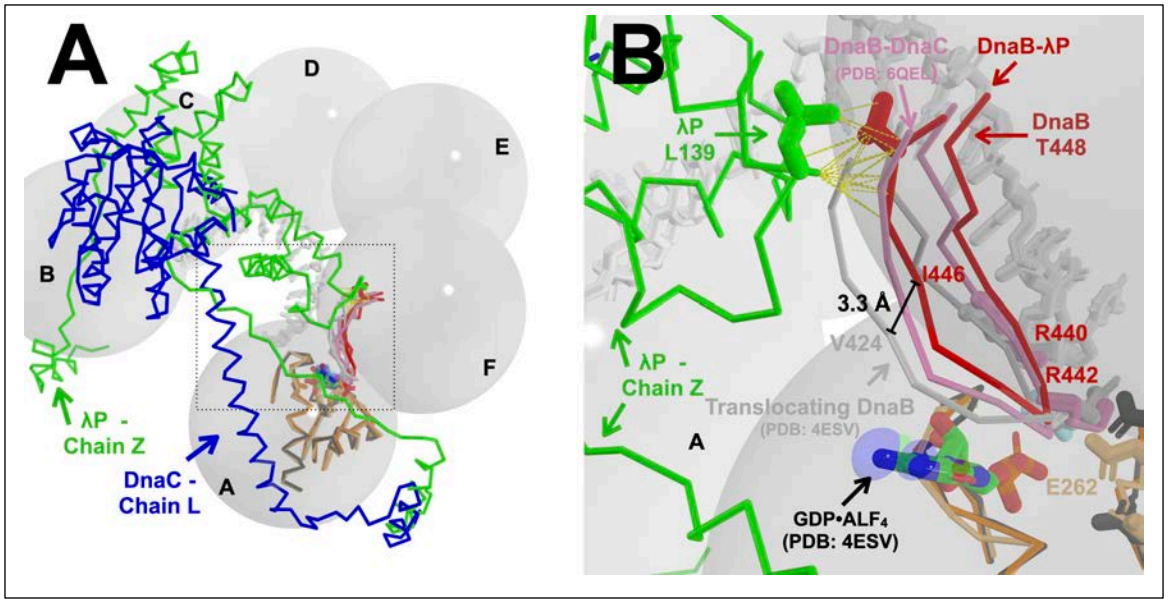

Figure 7. Misalignment of the ATPase centers in the DnaB open spiral. A) Transition to the open spiral form of DnaB leads to a misalignment of the ATPase center at the interface between two CTDs. Schematic view of the BP complex wherein the CTDs in the open spiral are represented by transparent and labeled grey spheres. Chain Z of the λP ensemble (green) is shown in the PyMol ribbon representation, as are portions of the CTDs from chain A (light orange) and chain F (salmon). B) Closeup (and rotated) portion of the pose in panel A is shown within the dotted-line square. Colored in red is a ribbon representation of the arginine finger beta-hairpin of chain F of the current BP structure. The corresponding elements from the *E. coli* DnaB-DnaC (PDB: 6QEL [41]) and *B.st* DnaB-ssDNA ([26]) structures are colored in pink and grey respectively. The ssDNA from the translocating *B.st* DnaB-ssDNA appears in grey in the background. Several residues in λP and DnaB in the BP complex are shown in stick format.

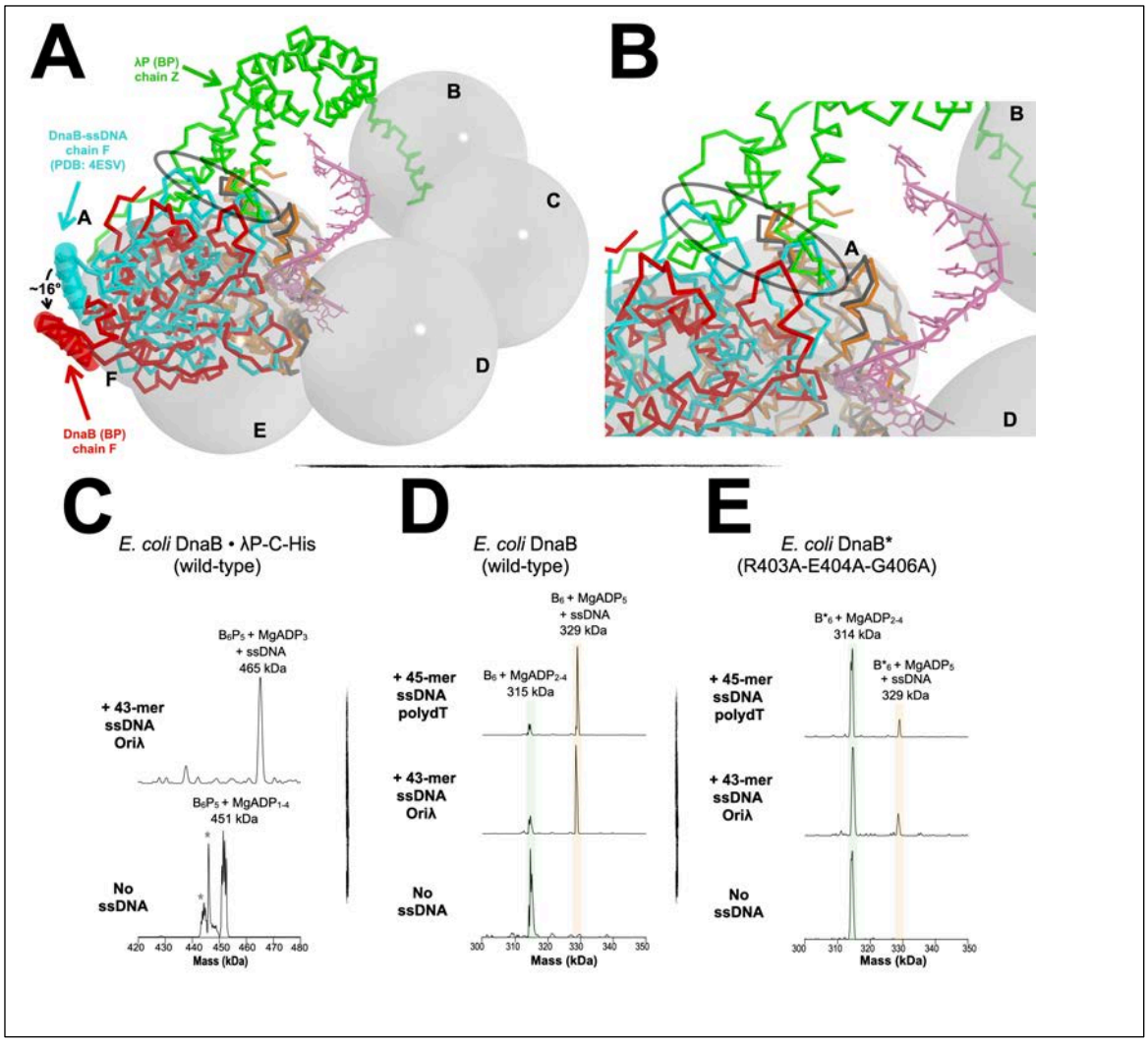

Figure 8. Does BP complex bind ssDNA initially outside the inner chamber of DnaB? A) Disposition of domain III of the λP loader in the BP complex precludes adoption by DnaB of the configuration competent of binding ssDNA. DnaB chain A (grey background) of the 4ESV structure ssDNA ([26]) is superimposed on DnaB chain A (orange, background) of the BP complex using residues 206:471 but omitting the DH (residues 290:306) and LH (181:196) helices from the calculation. In the foreground appear chains F of DnaB from the BP (red) and 4ESV (cyan) complexes, respectively; these two chains were also omitted

from the superposition. The ssDNA from the DNA complex (pink) is depicted using the PyMol sticks representation. The volume of the clash between the λP loader and the position of the CTD from the ssDNA complex is circled in each panel. The open DnaB spiral within the BP complex is represented by transparent and labeled grey spheres. Chain Z of the λP ensemble (green) is shown in the PyMol ribbon representation. B) Closeup of panel A. C-E) Native MS characterization of ssDNA-binding for E. coli DnaB and DnaB – λP-CHis. Deconvolved spectra for WT *E. coli* DnaB- λP-CHis (C), WT DnaB (D), triple mutant R403A E404A G406A DnaB (E), incubated with or without ssDNA. Multiple MgADP-bound states were observed for the DnaB hexamers (see Supplementary Table 4 for mass assignments). The DnaB samples were incubated with 0.5 mM ATP and a 1.2x-fold excess of ssDNA before buffer exchange into 500 mM ammonium acetate, 0.5 mM magnesium acetate, 0.01% Tween-20, and subsequent native MS analysis.

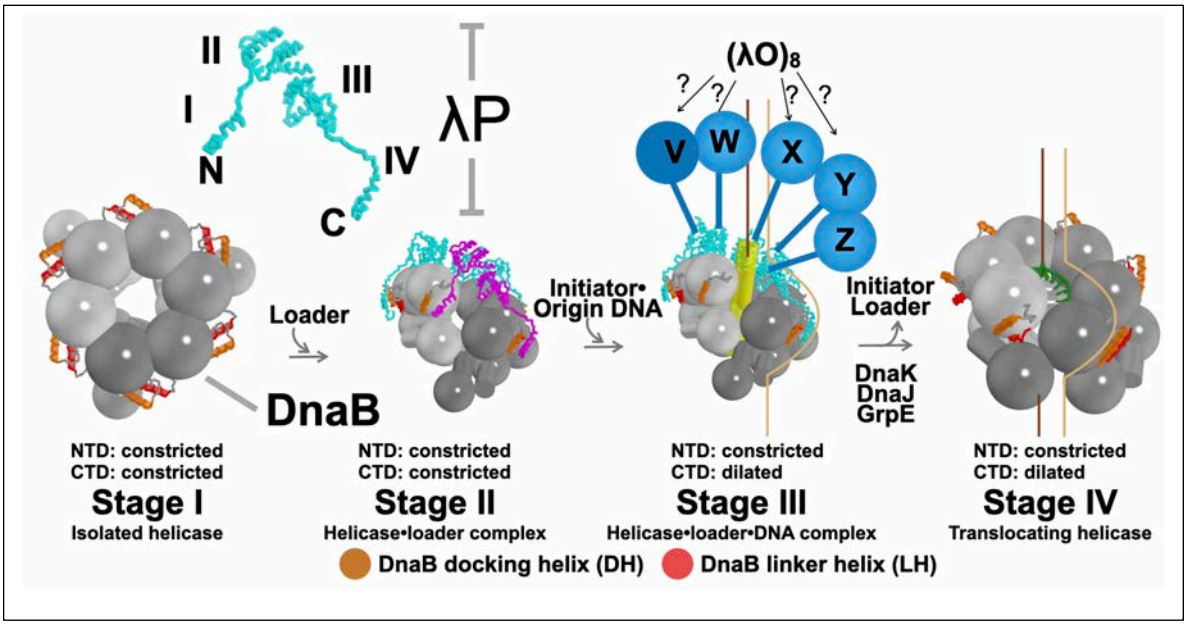

Figure 9. Model for Loading of the DnaB-λP loader complex to the λO-Oriλ.

The stages of assembly of the DnaB helicase at phage λ origin. In Stage II, five copies of the λP loader bind to the closed planar ring (Stage I) of *E. coli* DnaB and reconfigure it into an open spiral with openings in the NTD and CTD layers sufficient to allow ssDNA to enter the central chamber. However, one copy of the λP loader (magenta) binds on both sides of the breached interface in DnaB; this configuration effectively blocks entry to DnaB's inner chamber. Even though the path is blocked, the BP complex, nevertheless, binds ssDNA; it is suggested that ssDNA is bound outside the inner chamber of DnaB in Stage III. Expulsion of the λP loader from the complex on DNA, with the assistance of *E. coli* chaperone proteins, enables transition to Stage IV, the translocating form. The yellow cylinder represents the expected path of ssDNA as inferred from comparison to the DnaB•DnaC-ssDNA complex (PDB: 6QEM).